processes

MDPI

Article

Physics-Informed Neural Network Prediction of Nanofluid Thermal Transport in TPMS Gyroid Heat Exchangers

Mohammed Yahya * and Mohamad Ziad Saghir

Department of Mechanical, Industrial and Mechatronics Engineering, Toronto Metropolitan University, Toronto, ON M5B 2K3, Canada

* Correspondence: mohammed.yahya@torontomu.ca

Abstract

Triply periodic minimal surface (TPMS) heat exchangers offer high surface-area-to-volume ratios and interconnected flow pathways, making them attractive for compact thermal management. However, accurately predicting nanofluid heat transfer over a wide range of nanoparticle concentrations and operating conditions in complex TPMS geometries remains computationally challenging because of the coupled effects of porous architecture, flow dynamics, and concentration-dependent thermophysical properties. In this study, a hybrid physics-informed neural network (PINN) framework was developed to reconstruct concentration-dependent Al_2O_3–*water* nanofluid temperature fields in TPMS gyroid heat exchangers. The originality of the proposed approach lies in integrating sparse thermocouple measurements, a steady-state convection–diffusion equation, boundary condition residuals, concentration-dependent nanofluid property models, and a physics-based concentration scaling procedure within a unified framework. The proposed framework was applied to aluminum and silver TPMS heat exchangers over a wide range of nanofluid volume fractions and flow conditions. The trained PINN accurately reconstructed the experimentally measured temperature field, demonstrating excellent agreement with the reference experimental data. Predictions at concentrations beyond the experimentally measured reference condition were obtained using the physics-based concentration scaling model. The effective heat transfer coefficient and Nusselt number were subsequently evaluated from the predicted mean TPMS temperature through an energy balance formulation. Increasing nanoparticle concentration reduced the predicted TPMS temperatures by approximately 17.5–18.5%, while the combined increase in concentration and flow rate produced an overall temperature reduction of about 33.5%. Relative to the selected baseline condition, the combined variation in concentration and flow rate was associated with calculated increases of 62.08% in h_{eff}, 58.33% in Nu, and 59.32% in Re. These results demonstrate the potential of the proposed hybrid PINN framework as a computationally efficient surrogate for evaluating nanofluid-enhanced TPMS heat exchangers, while acknowledging that predictions away from the training concentration depend on the validity of the concentration scaling model.

Keywords: TPMS structures; heat transfer; heat exchangers; inverse heat conduction; physics-informed neural network and machine learning

Academic Editor: Marek Markowski

Received: 7 July 2026
Revised: 10 August 2026
Accepted: 13 August 2026
Published: 13 August 2026

1. Introduction

Modern thermal systems require compact and efficient heat exchangers capable of removing high heat fluxes under limited flow and space conditions. Conventional designs,

such as straight channels, pin fins, and simple porous media, are increasingly limited by their geometry and relatively low surface-area-to-volume ratios [1–3]. This has motivated growing interest in architected porous structures that can improve heat transfer pathways and thermal performance.

TPMS structures are promising candidates for advanced heat exchangers because they provide continuous interconnected channels, high surface-area-to-volume ratios, and smooth geometries [4,5]. TPMS topologies, such as gyroid, Schwarz-D, and diamond surfaces, are periodic in three spatial directions and provide complex but continuous flow pathways [6]. Among them, the gyroid structure is particularly attractive due to its geometric continuity, structural uniformity, and suitability for additive manufacturing [7]. These characteristics enhance the interaction between solid conduction and fluid convection while improving thermal uniformity compared with many conventional porous structures [8–10].

Nanofluids provide an additional method for improving heat transfer performance. By dispersing high-conductivity nanoparticles, such as Al_2O_3, CuO and TiO_2 or carbon-based materials, into a base fluid, the effective thermal conductivity and convective heat transfer capability of the working fluid can be enhanced [11–14]. Several studies have reported improved heat transfer coefficients and Nusselt numbers when nanofluids are used in channels, microchannels, and porous media, particularly under flow conditions where conduction effects are important [15–18].

However, nanofluid behaviour is strongly affected by nanoparticle concentration, particle material, particle size, dispersion stability, viscosity increase, and flow conditions [19]. These effects become more complex when nanofluids flow through TPMS geometries, where porous architecture, flow distribution, and thermal gradients are strongly coupled. As a result, conventional heat transfer correlations may not fully capture the combined effects of TPMS geometry and concentration-dependent nanofluid properties [20].

Although TPMS heat exchangers and nanofluids each offer significant thermal advantages, their combined behaviour is difficult to predict using experiments or high-fidelity simulations alone. Experiments over multiple nanoparticle concentrations and flow rates are time-consuming, while detailed numerical simulations of TPMS domains require fine meshes and high computational cost. Therefore, surrogate modelling approaches, particularly machine learning and physics-informed neural networks, offer a promising route for predicting nanofluid thermal transport in TPMS heat exchangers with reduced experimental and computational effort.

Recent advances in machine learning (ML) have transformed the prediction of complex engineering systems by enabling accurate approximation of highly nonlinear relationships directly from experimental and numerical datasets. Compared with conventional empirical correlations, ML techniques can identify hidden patterns in multidimensional data and provide rapid predictions without repeatedly solving computationally intensive governing equations. Consequently, ML has been successfully applied to material design, structural analysis, manufacturing processes, and thermal fluid systems.

Akbari et al. [21] applied ML to predict the mechanical properties of metal additive-manufactured components using a comprehensive experimental dataset. Their results demonstrated that machine learning can provide accurate predictions while reducing the need for extensive experiments and computationally expensive simulations. Deng et al. [22] employed ML to predict the mechanical properties of Cu–Al alloys, demonstrating that data-driven models can accurately capture complex material behaviour while significantly reducing computational effort. Similarly, Imran et al. [23] used ML techniques to estimate the mechanical properties of carbon nanotube-incorporated concrete, showing that machine learning provides reliable predictions even for highly nonlinear engineering problems.

Among ML approaches, artificial neural networks (ANNs) have become one of the most widely adopted tools for modelling thermal systems because of their ability to learn nonlinear input–output relationships from experimental data. Ewim et al. [24] reviewed the application of ANNs in thermal engineering and concluded that ANN models provide accurate predictions for a wide range of heat transfer and energy-system applications while substantially reducing computational cost compared with conventional numerical simulations. Ibrahim et al. [25] further demonstrated the capability of ANN models for predicting convective heat transfer of nanofluids in enclosed cavities, where the trained network successfully captured the influence of flow regime and nanoparticle concentration on the thermal behaviour.

Despite their excellent predictive capability, conventional ANN models rely entirely on training data and do not explicitly enforce the governing physical laws. As a result, their predictive accuracy and generalization capability often deteriorate when extrapolating beyond the available experimental dataset or when only limited measurements are available. To address these limitations, physics-informed neural networks (PINNs) were introduced by Raissi et al. [26], who incorporated the governing partial differential equations directly into the neural network loss function. By simultaneously satisfying experimental observations and physical constraints, PINNs provide physically consistent solutions for both forward and inverse problems involving nonlinear partial differential equations. Since then, PINNs have emerged as a powerful scientific machine learning framework for solving multiphysics problems while requiring significantly fewer training data than conventional neural networks.

The rapid development of PINNs has led to numerous extensions for complex engineering applications. Cuomo et al. [27] presented a comprehensive review of scientific machine learning based on PINNs, highlighting their effectiveness in solving inverse problems, data assimilation, uncertainty quantification, and multiphysics simulations. The review also identified sparse-data reconstruction, computational efficiency, and complex geometries as key research challenges. More recently, Uhrich et al. [28] demonstrated the application of physics-informed deep learning for real-time anomaly detection and fault mitigation in additive manufacturing, illustrating the capability of physics-informed learning to combine measurement data with governing physical principles for accurate real-time prediction in engineering systems.

Although significant progress has been achieved in ANN- and PINN-based modelling, their application to nanofluid heat transfer in TPMS gyroid heat exchangers remains limited. In particular, few studies have integrated sparse experimental measurements, concentration-dependent nanofluid thermophysical properties, governing heat transfer equations, and TPMS geometries within a unified physics-informed learning framework. The present study addresses this gap by developing a hybrid PINN framework that reconstructs the TPMS temperature field from sparse experimental data and extends the predictions to a wide range of nanofluid concentrations using a physics-based concentration scaling approach, thereby providing an efficient surrogate model for TPMS heat exchangers.

PINNs, a subset of neural network-based machine learning models, provide an effective approach for combining data-driven learning with physical laws. Unlike conventional neural networks that rely only on training data, PINNs include governing partial differential equations, constitutive relations, and boundary condition constraints directly in the loss function. This helps ensure that the predicted solution remains consistent with energy conservation and heat transfer physics. PINNs have been widely applied to forward and inverse heat transfer problems, especially in complex geometries where traditional numerical simulations can be computationally expensive or difficult to implement. Yahya et al. [29] developed a PINN model to predict thermal behaviour in porous TPMS metals. Their

work showed that PINNs can reconstruct temperature fields from limited experimental data, generalize predictions across different materials, and estimate heat transfer quantities where direct measurements are not available. El Hassan et al. [30] reviewed the application of PINNs in fluid dynamics using sparse experimental and numerical data. The authors showed that PINNs improve prediction accuracy by embedding governing physical equations into the learning process, enabling accurate reconstruction of flow fields while reducing the dependence on large datasets. The review also highlighted data-driven PINNs as a promising approach for complex engineering applications involving limited measurements. Zhang et al. [31] proposed MUSA-PINN, a multi-scale weak-form physics-informed neural network for fluid flow in complex TPMS geometries. Their proposed framework enforces conservation laws over multi-scale control volumes, improving prediction accuracy and physical consistency in complex flow passages. The method demonstrated superior performance to existing PINN models for TPMS heat-exchanger channels, highlighting the potential of advanced PINN formulations for complex thermal fluid engineering applications. Bobbili et al. [32] developed a PINN to predict the high-strain-rate energy absorption of LPBF-fabricated lattice structures. By embedding the linear elastic constitutive relation into the loss function, the PINN achieved higher prediction accuracy and better generalization than conventional machine learning models, demonstrating the effectiveness of physics-informed learning for complex lattice geometries.

Motivated by the findings reported in the literature, the present study develops a PINN framework for predicting Al_2O_3 nanofluid thermal transport in TPMS gyroid heat exchangers over different nanoparticle concentrations and flow rates. The framework combines experimental thermocouple measurements, concentration-dependent nanofluid property models, governing convection–diffusion heat transfer physics, and heat transfer scaling relations. This allows the model to predict temperature distributions, effective heat transfer coefficients, and Nusselt numbers in a physically consistent way, while reducing the need for extensive experiments or high-cost simulations. The developed framework is considered a hybrid forward–inverse model. The forward component comes from predicting temperature fields using known inputs, including spatial coordinates, flow rate, nanoparticle concentration, material conductivity, nanofluid properties, pore velocity, and effective porous thermal conductivity. The inverse component comes from using sparse thermocouple measurements to reconstruct the continuous temperature field within the TPMS domain. Therefore, the model acts as a physics-informed forward surrogate with inverse temperature-field reconstruction capability, allowing predictions beyond the directly measured cases while remaining consistent with experimental data and heat transfer physics.

Unlike conventional PINN implementations, which are generally trained and applied at fixed material properties and operating conditions, the proposed framework incorporates concentration-dependent thermophysical property models and a physics-based concentration scaling strategy to extend the reconstructed temperature field beyond the experimentally measured reference condition.

2. Theoretical Background

2.1. Triply Periodic Minimal Surfaces

TPMS are a class of mathematically defined, bicontinuous surfaces characterized by zero mean curvature at every point and periodic repetition in three orthogonal directions [33]. The zero-mean-curvature property means that the two principal curvatures κ_1 and κ_2 at every surface point are equal in magnitude but opposite in sign $\kappa_1 + \kappa_2 = 0$. This condition minimizes surface area for a given boundary, endowing TPMS structures with exceptionally high surface-area-to-volume ratios and mechanically efficient load

paths [34,35]. Their bicontinuous architecture creates two interpenetrating, non-intersecting channels that simultaneously allow fluid flow and solid heat conduction, which is considered an ideal configuration for compact heat exchangers.

The gyroid is one of the most widely studied TPMS geometries for thermal applications. The gyroid is a highly symmetric cubic space group and possesses no planes or axes of reflection symmetry, giving it superior mechanical isotropy relative to other TPMS types [35]. The TPMS gyroid geometry is described using the level-set formulation [36]:

$$\Phi(X, Y, Z) = cos(X)\cdot sin(Y) + cos(X)\cdot sin(Z) + cos(Z)\cdot sin(X) = C \quad (1)$$

where $X = 2\pi x$, $Y = 2\pi y$, and $Z = 2\pi z$ are the dimensionless Cartesian coordinates defining the three-dimensional periodic domain. The parameter C represents the geometric offset that controls the solid-void volume fraction. In the present study, $C = 0$ is selected to represent a single gyroid TPMS unit cell with symmetric solid and fluid domains and thereby controls porosity ε. For the gyroid used in this study, the porosity is ε = 0.70, meaning 70% of the total volume is available to the fluid [5].

2.2. Heat Transfer in Porous Media

The thermal behaviour of a fluid flowing through a solid porous matrix is rigorously described by volume-averaged transport equations. Volume averaging replaces the microscale solid–fluid interface conditions with macroscale effective properties, making the problem tractable without resolving individual pore geometries. The energy transport within the TPMS heat exchanger is described using the local thermal equilibrium (LTE) assumption, whereby the solid TPMS skeleton and the nanofluid are assumed to share a common local temperature field, such that $T_s = T_f = T$. Under this assumption, the separate solid and fluid energy equations reduce to a single effective energy equation,

$$\rho_{nf} C_{P,nf} u_p \frac{\partial T}{\partial x} = k_{eff}\left(\frac{\partial^2 T}{\partial x^2} + \frac{\partial^2 T}{\partial y^2} + \frac{\partial^2 T}{\partial z^2}\right) \quad (2)$$

here T is the common local temperature of the solid and fluid phases, u_p is the interstitial pore velocity vector, and ρ_{nf}, $C_{P,nf}$, and k_{eff} are the effective density, specific heat capacity, and thermal conductivity of the porous TPMS–nanofluid system, respectively. The left-hand side of Equation (2) represents convective transport of thermal energy by the nanofluid along the streamwise direction, whereas the right-hand side describes effective heat conduction within the porous medium in the axial (x), lateral (y), and transverse (z) directions. The effective thermal conductivity accounts for the combined conductive contributions of the interconnected TPMS solid skeleton and the nanofluid occupying the pore space.

The LTE assumption is considered appropriate for the present TPMS geometry and operating conditions because of the high thermal conductivity of the metallic TPMS structure and the relatively small temperature difference between the solid and fluid phases. The validity of this assumption is further assessed through the LTE–LTNE sensitivity analysis, where the influence of thermal non-equilibrium on the predicted temperature field and heat transfer performance is quantitatively evaluated.

Axial conduction is retained because the Péclet number (P_e) is not uniformly large across all tested flow rates [7].

$$P_e = \frac{\rho_{nf} C_{P,nf} u_{pore}}{k_{eff}} L \quad (3)$$

The Péclet number is a dimensionless parameter that compares convective heat transport with conductive heat transport in a porous medium. Here, L is the characteristic

length. A low P_e indicates diffusion-dominated heat transfer, whereas a high P_e indicates convection-dominated transport. Since P_e is not uniformly large across the investigated flow rates, forced convection does not fully suppress heat diffusion along the flow direction. Therefore, axial conduction remains relevant and is included in the governing energy equation. The pore velocity was used instead of the superficial average velocity because the TPMS structure behaves as a porous medium, where the fluid flows only through the interconnected pore space. In porous-media theory, the interstitial or pore velocity is obtained by correcting the superficial velocity by the porosity, $u_p = u_{avg}/\varepsilon = \varphi/A_c\varepsilon$, making it more representative of the actual fluid velocity inside the TPMS channels [37,38]. The effective thermal conductivity of the TPMS porous composite is modelled using a parallel (volume-averaged) mixture rule, which assumes that heat is conducted simultaneously through the solid ligaments and the nanofluid occupying the pore space [39].

$$k_{eff} = (1 - \varepsilon)k_s + \varepsilon k_{nf} \tag{4}$$

where k_s is the thermal conductivity of the solid skeleton material and k_{nf} is the concentration-dependent nanofluid thermal conductivity. The parallel model provides an upper bound on effective conductivity and is appropriate for TPMS geometries where both the solid and fluid phases form fully interconnected continuous networks.

2.3. Al_2O_3–Water Nanofluid Thermophysical Properties

Nanofluids are colloidal suspensions of nanometre-scale particles ($\leq$1 µm) in a conventional base fluid [40]. Nanofluid thermal enhancement is not governed only by classical mixture effects but may also be influenced by nanoscale mechanisms such as Brownian motion, thermophoresis, and nanolayer formation. Brownian motion refers to the random movement of nanoparticles within the base fluid, which can promote microscopic mixing and energy transport. Thermophoresis describes nanoparticle migration under temperature gradients, typically from hotter regions toward colder regions, which can affect local particle distribution near heated surfaces. Nanolayer effects arise from the ordered liquid layer formed around nanoparticle surfaces, which can modify interfacial heat conduction and contribute to the effective thermal conductivity of the suspension. Therefore, the addition of high-conductivity nanoparticles can enhance the thermal conductivity of the base fluid beyond that predicted by simple classical mixture theory. Among different nanoparticle materials, Al_2O_3 nanoparticles are widely used because of their chemical stability, low cost, and moderate thermal conductivity compared with metallic nanoparticles [41,42].

The nanofluid density follows the linear mixture rule, derived from conservation of mass for a two-component system [43]:

$$\rho_{nf} = (1 - \varphi)\rho_f + \varphi\rho_p \tag{5}$$

The nanofluid density was calculated using a volume-fraction-based mixture relation, where the effective density depends on the relative contributions of the base fluid and the suspended nanoparticles. Here, φ is the nanoparticle volume concentration, where $(1 - \varphi)\rho_f$ represents the contribution of the base fluid, while $\varphi\rho_p$ represents the contribution of the nanoparticles. As φ increases, more nanoparticles are added to the fluid, so the nanofluid density increases because Al_2O_3 particles are denser than water.

The effective specific heat capacity is obtained by equating the volumetric thermal energy storage of the nanofluid to that of its components [43]. This equation shows how much heat the nanofluid can store after nanoparticles are added to the base fluid. Since

Al_2O_3 nanoparticles usually have a lower specific heat capacity than water, increasing φ often reduces the overall $C_{p,nf}$.

$$C_{p,nf} = \frac{(1-\varphi)\rho_f C_{p,f} + \varphi\rho_p C_{p,p}}{\rho_{nf}} \tag{6}$$

The dynamic viscosity of the nanofluid is described by the Brinkman model [44,45], which extends Einstein's formula for dilute suspensions to moderate particle volume fractions:

$$\mu_{nf} = \frac{\mu_f}{(1-\varphi)^{2.5}} \tag{7}$$

where $\mu_{nf} = 1.0 \times 10^{-3}$ Pa·s is the base fluid dynamic viscosity. The nanofluid viscosity was estimated using the Brinkman model, which accounts for the increase in flow resistance caused by suspended nanoparticles. As the nanoparticle volume concentration increases, the effective viscosity of the nanofluid increases, which may affect the Reynolds number, pressure drop, and pumping-power requirements, which is a key penalty that must be balanced against thermal enhancement in heat exchanger design. At $\varphi = 2.5\%$ vol the model predicts approximately a 6.7% increase in viscosity relative to pure water [40,45].

Finally, the thermal conductivity of the nanofluid is calculated using the Maxwell model for spherical particles. This model estimates the effective thermal conductivity of a suspension containing solid spherical particles dispersed in a continuous liquid medium. It is derived from potential theory for dilute suspensions of non-interacting particles and is commonly used to describe how high-conductivity nanoparticles modify the thermal conductivity of the base fluid. As the nanoparticle volume concentration, φ, increases, the contribution of the particles becomes more significant. Since Al_2O_3 has a higher thermal conductivity than water, the effective nanofluid thermal conductivity, k_{nf}, increases with increasing nanoparticle concentration [46]:

$$k_{nf} = k_f \frac{k_p + 2k_f + 2\varphi(k_p - k_f)}{k_p + 2k_f - \varphi(k_p - k_f)} \tag{8}$$

The Maxwell model is theoretically exact in the dilute limit (φ = 0) and has been extensively validated for Al_2O_3–*water* nanofluids at volume fractions up to approximately 5% [19,42]. For $\varphi \ll 1$, Equation (8) reduces to the linear approximation $k_{nf} \approx k_f\left[1 + 3\varphi\left(\frac{k_p}{k_f} - 1\right)\right]$, confirming that conductivity enhancement scales linearly with concentration at low φ However, in the present study, the full Maxwell model [46] was used to retain the concentration-dependent behaviour more accurately.

3. Methodology

The proposed hybrid PINN framework consists of several interconnected components, including the governing heat transfer equations, boundary conditions, experimental data integration, physics-informed neural network formulation, concentration scaling model, and post-processing of thermal performance parameters. For clarity, Table 1 summarizes these components before their detailed mathematical formulation and implementation are presented in the subsequent subsections.

Figure 1 illustrates the overall computational workflow of the proposed hybrid PINN framework. The procedure begins with the acquisition of experimental temperature measurements and operating conditions, followed by data preprocessing and PINN training using the governing heat transfer equation and boundary condition constraints.

Table 1. Summary of the governing equations, boundary conditions, PINN formulation, concentration scaling model, and dimensionless parameters used in the proposed framework.

Component	Description
Governing equation	Steady-state convection–diffusion equation under LTE
Boundary conditions	Inlet temperature, prescribed heat flux, outlet zero-gradient condition
PINN outputs	TPMS temperature field
Experimental inputs	Seven thermocouple temperatures at five flow rates
Physics constraints	PDE residual + boundary condition residual
Concentration scaling	Reynolds–Prandtl–thermal conductivity scaling
Heat transfer evaluation	Energy balance formulation for h_{eff} and Nu
Dimensionless numbers	Reynolds, Prandtl, Nusselt

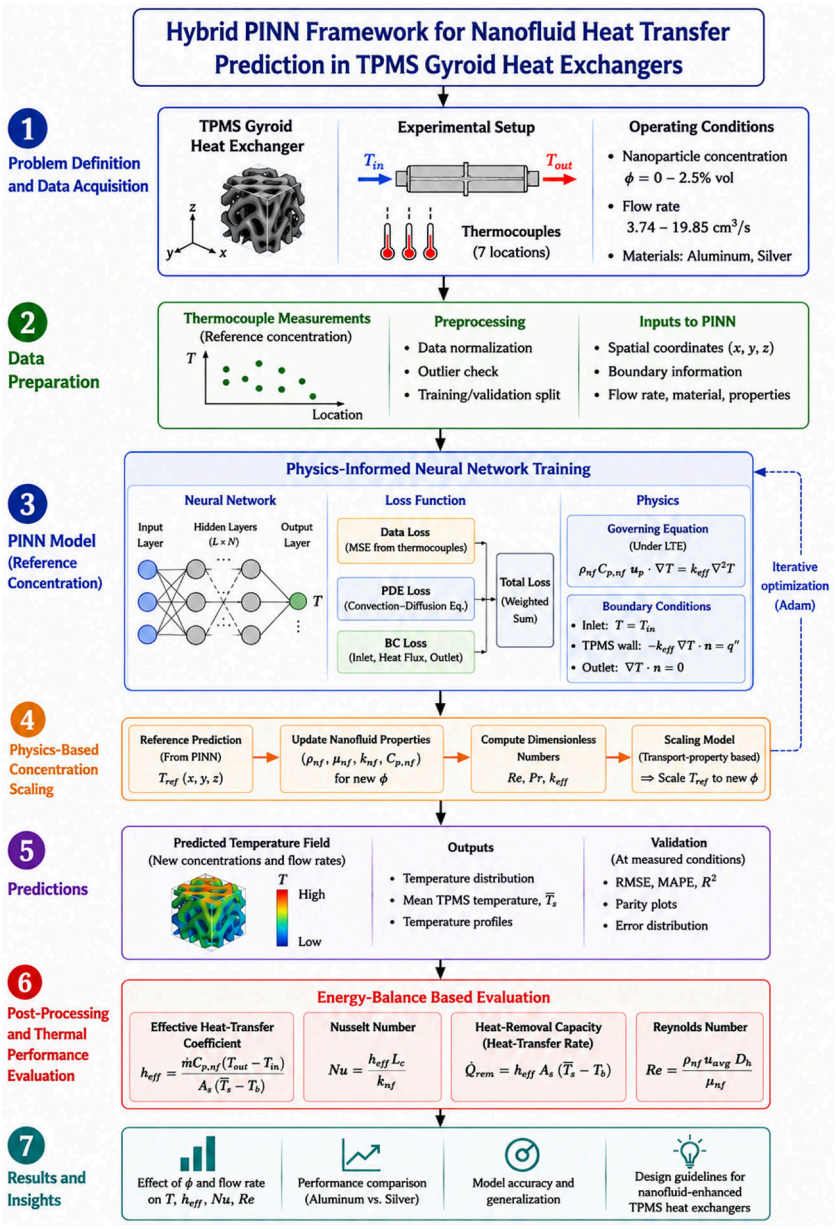

Figure 1. Computational workflow of the proposed hybrid PINN framework for TPMS gyroid heat exchangers.

The trained PINN reconstructs the reference TPMS temperature field, which is subsequently extended to other nanoparticle concentrations through the physics-based concentration scaling model. Finally, the predicted temperature field is used to evaluate the

effective heat transfer coefficient, Nusselt number, and other thermal performance metrics using an energy balance formulation.

3.1. TPMS Geometry and Experimental Configuration

A PINN model was developed to predict the temperature distribution in a TPMS gyroid structure cooled by an Al_2O_3–*water* nanofluid flowing through the porous TPMS domain. The model combines sparse experimental thermocouple measurements with a physics-based porous through-flow energy equation. The main objective is to establish the relationship between nanoparticle volume concentration and the temperature profile inside the TPMS region and then use the trained model to predict temperature distributions at higher Al_2O_3 concentrations. The developed model is used to learn the measured temperature response of aluminum and silver TPMS samples at the experimental nanofluid concentration of, $\varphi = 0.6\%$ vol, and then predict the temperature field at higher nanofluid volume fractions. This value corresponds to $\varphi_{ref} = 0.6\%$ vol Al_2O_3 nanoparticle volume concentration used as a reference experimental nanofluid concentration during the PINN training. After the training, the model is evaluated at the following concentration values of 0.2%, 0.4%, 0.6%, 1.0%, 1.4%, 1.8%, 2.0% and 2.5% Al_2O_3 nanoparticle volume fraction.

The working fluid is modelled as Al_2O_3 nanoparticles dispersed in water. The thermophysical properties of the Al_2O_3–*water* nanofluid are evaluated as functions of nanoparticle volume concentration. Specifically, concentration-dependent correlations are used to calculate the effective density, viscosity, specific heat capacity, and thermal conductivity. These property variations account for the influence of nanoparticle addition on the thermal and flow behaviour of the base fluid. In the present MATLAB® R2026b model, the Al_2O_3–*water* cooling fluid properties are defined in Table 2 [47].

Table 2. Thermo-physical properties of the water and Al_2O_3 nanoparticles.

	ρ [kg/m^3]	μ [Pa·s]	C_P [J/kg·K]	K [W/m·K]
Water	997	-	4182	0.6
Al_2O_3	3950	0.001	765	35

The nanofluid thermophysical properties were evaluated as functions of nanoparticle volume concentration using the standard mixture-based correlations given in Equations (5)–(8). These correlations account for the contribution of the base fluid and dispersed nanoparticles to the effective density, specific heat capacity, thermal conductivity, and dynamic viscosity of the nanofluid. As the nanoparticle concentration increases, the resulting effective properties vary accordingly, influencing both the convective and conductive heat transfer behaviour of the working fluid.

These concentration-dependent properties are then incorporated into the PINN and the heat transfer post-processing model. In the PINN framework, they provide the material-property inputs required to represent the thermal response of the nanofluid under different flow and concentration conditions. In the post-processing stage, the same properties are used to calculate the relevant heat transfer parameters, ensuring consistency between the governing thermal model, the learned temperature field, and the final performance evaluation.

The solid TPMS material is represented through its thermal conductivity. Two solid materials are included in the MATLAB model; the thermal conductivities of the aluminum and the silver are $k_{Al} = 237$ W/m·K and $k_{Si} = 429$ W/m·K, respectively [47].

The effective porous thermal conductivity of the TPMS region is calculated using a porosity-weighted relation given in Equation (4), which represents the combined contribution of the solid TPMS structure and the nanofluid inside the pore volume. However,

because the solid thermal conductivity is much larger than the nanofluid thermal conductivity, k_{eff} is strongly dominated by the solid material. Therefore, the change in k_{nf} with increasing nanoparticle concentration causes only a limited change in k_{eff}. For this reason, the present corrected model also includes a Nusselt number enhancement factor to represent the stronger convective heat transfer improvement reported in nanofluid studies.

In the present PINN model, the full three-dimensional TPMS thermal behaviour is represented using a two-dimensional x-z temperature field. The TPMS specimens were fabricated in a square cross-sectional geometry with an overall length of $L = 37.5$ mm and a height of $H = 12.7$ mm. All samples were manufactured with a constant porosity of $\varepsilon = 0.7$, corresponding to a relative density of 0.3. The geometric characteristics include a unit-cell size of 10 mm and a total fluid-solid interfacial surface area of 15.524 cm^2. The TPMS structure was represented as an effective three-dimensional porous domain in the streamwise vertical plane. The flow direction was taken along the *x-axis*, from left to right. The coordinate system was defined such that $x = 0$ corresponds to the inlet side of the TPMS sample and $x = L$ corresponds to the outlet side, while the vertical heat transfer direction was represented by the *z-axis*, such that $z = 0$ corresponds to the heated base surface and $z = H$ corresponds to the upper boundary of the porous TPMS domain. The thermocouples were located 1 mm below the TPMS interface. Therefore, their vertical coordinate in the computational domain was $z_{TC} = -1$ mm, thus, the thermocouple measurement plane was $z_{TC} = -1.0 \times 10^{-3}$ m.

Experiments were performed in a closed-loop thermal-hydraulic facility, shown schematically in Figure 2a. The working fluid was circulated by a variable-speed pump, and the volumetric flow rate was regulated using a precision control valve prior to entering the heated test section. The TPMS insert was mounted on a uniformly heated aluminum base block, which supplied a constant surface heat flux of 38.4 kW/m^2 to the porous structure.

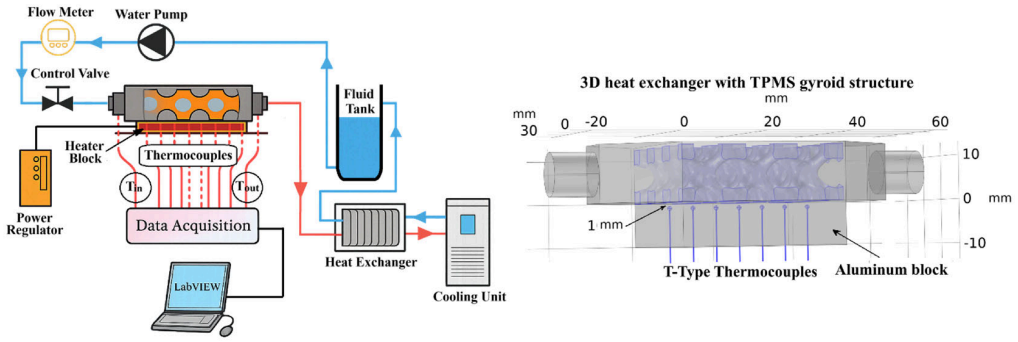

Figure 2. (**a**) Schematic of the closed-loop thermal–hydraulic experimental facility, showing fluid circulation, controlled heat input to the TPMS gyroid test section, thermocouple instrumentation, and real-time data acquisition using LabVIEW 2013. (**b**) Arrangement of T-type thermocouples embedded 1 mm below the TPMS–fluid interface for interfacial temperature measurements.

Temperature measurements were obtained using seven T-type thermocouples (manufacturer-specified accuracy ±0.5 °C) embedded in the aluminum base at a fixed depth of 1 mm below the TPMS–fluid interface.

The sensors were distributed along the streamwise direction at $y = 0$, with the first located at $x = 2.3$ mm from the inlet and uniformly spaced at 5.5 mm intervals, such as $x_{TC} = [2.3, 7.8, 13.3, 18.8, 24.3, 29.8, 35.3]$ mm, as illustrated in Figure 2b, enabling detailed characterization of the interfacial thermal response.

Forced convection experiments were conducted using nanofluids at a reference nanoparticle volume fraction of $\varphi_{ref} = 0.6\%$ vol, for five volumetric flow rates of $\varphi = [3.74, 7.786, 11.8, 15.73, 19.85]$ cm^3/s.

The inlet and outlet bulk fluid temperatures were maintained at $T_{in} = 11$ °C and $T_{out} = 13$ °C, respectively. The experimentally measured TPMS interface temperatures at φ_{ref} used as the anchor dataset for all subsequent modelling and predictive analysis. Temperature signals were acquired using a data-acquisition system and monitored in real time via a LabVIEW-based interface. After exiting the test section, the fluid was cooled and returned to the storage reservoir, completing the circulation loop. All experiments were conducted under controlled laboratory conditions with an ambient reference temperature of 23 °C, following the validated methodology reported in Ref [36].

3.2. Physical Description and Assumptions

The thermal system investigated in this study consists of a TPMS gyroid heat exchanger subjected to a uniform heat flux at the solid–fluid interface and cooled by a nanofluid flowing through the interconnected porous channels. The gyroid topology provides a continuous, smooth internal surface that promotes strong coupling between conduction in the solid skeleton and convection within the fluid domain.

The analysis is restricted to steady-state conditions. The flow is assumed to be laminar, incompressible, and Newtonian. Thermal radiation and viscous dissipation are neglected. The nanofluid is modelled as a single-phase effective medium in which nanoparticles are uniformly dispersed within the base fluid, and slip effects between the solid and fluid phases are ignored. Thermophysical properties are assumed constant for a given nanoparticle concentration. These assumptions are consistent with widely adopted modelling approaches for nanofluid heat transfer in laminar porous flows and enable a tractable yet physically meaningful formulation.

4. Physics-Informed Neural Network (PINN) Architecture

Conventional PINN formulations have been successfully applied to forward and inverse heat transfer problems where the governing equations and boundary conditions are sufficient to predict the solution over the domain of interest. In the present study, however, the available experimental dataset is limited to sparse temperature measurements obtained at a single reference nanoparticle concentration. Consequently, a conventional PINN trained solely on these measurements would reconstruct the temperature field only for the reference operating condition and would not directly predict the influence of varying nanoparticle concentration on the thermal response. To address this limitation, the proposed framework integrates the PINN with concentration-dependent nanofluid property models and a physics-based concentration scaling procedure, enabling physically consistent prediction of temperature fields over a wider range of nanoparticle concentrations while preserving the governing heat transfer physics.

The developed PINN in this study was used to predict the temperature field of TPMS gyroid heat exchangers under different flow rates, nanoparticle concentrations, and material conditions. The proposed network is based on a multilayer perceptron (MLP) architecture, which is suitable for modelling complex nonlinear relationships between input and output variables. In the present work, this nonlinear behaviour results from the coupled effects of flow rate, nanofluid thermophysical properties, nanoparticle concentration, solid thermal conductivity, and heat transfer inside the porous TPMS structure.

The network consists of an input layer, several hidden layers, and an output layer. The input layer receives the spatial coordinates and operating parameters, including x, z, volumetric flow rate, nanoparticle concentration, solid thermal conductivity, nanofluid density, specific heat capacity, thermal conductivity, viscosity, pore velocity, and effective porous thermal conductivity. The output layer predicts the local temperature field, T(x,z). The hidden layers contain trainable neurons that transform the input variables through

nonlinear activation functions, allowing the network to learn the relationship between the operating conditions and the resulting temperature distribution. Unlike a conventional data-driven neural network, the PINN does not rely only on minimizing the difference between predicted and experimental temperatures. Instead, the governing convection–diffusion heat transfer equation and boundary condition residuals are embedded into the loss function. During training, the network weights are updated to satisfy both the experimental thermocouple measurements and the underlying heat transfer physics. The total loss function includes the data loss, which measures the error between predicted and measured thermocouple temperatures, and the physics losses, which enforce the governing PDE and boundary conditions.

The experimental data obtained from aluminum and silver TPMS gyroid samples tested with pure water and the reference $\varphi_{ref} = 0.6\%\ Al_2O_3$ nanofluid were used to train and validate the model. The data were normalized before training to improve numerical stability and convergence. The network was trained iteratively using gradient-based optimization, where the prediction error and physics residuals were back-propagated through the network to update the trainable weights and biases. This process continued until the total loss was minimized and stable convergence was achieved.

The trained PINN was then used as a surrogate model to predict temperature profiles beyond the directly measured cases. In particular, it was used to estimate the thermal response of the TPMS heat exchanger over nanoparticle concentrations ranging from $\varphi = 0$ to $\varphi = 2.5\%$ vol and flow rates from 3.74 to 19.85 cm^3/s. This structure allowed the model to capture both the experimental trends and the physical constraints of heat transfer, making it suitable for predicting concentration-dependent nanofluid thermal transport in TPMS gyroid heat exchangers.

4.1. Governing Energy and Boundary Equations

Heat conduction within the solid TPMS structure is governed by the steady-state Fourier heat conduction equation,

$$k_s\left(\frac{\partial^2 T_s}{\partial x^2} + \frac{\partial^2 T_s}{\partial z^2}\right) = 0 \tag{9}$$

Here k_s denotes the thermal conductivity of the TPMS solid material, and T_s is the local solid temperature field. The energy transport within the nanofluid flowing through the TPMS channels is described by the steady-state convection–diffusion equation.

When the thermal response times of the solid structure and the fluid are comparable, and the interfacial heat exchange between them is sufficiently strong, the LTE assumption can be applied.

The applicability of the local thermal equilibrium approximation was assessed using characteristic Biot numbers and thermal response times. The specific solid–fluid interfacial area was calculated as $a_{sf} = A_s/V = 256.7\ cm^{-1}$. A characteristic solid length was estimated as $L_s = (1-\varepsilon)/a_{sf} = 1.17$ mm. Using the effective heat transfer coefficients obtained from the reference-condition energy balance, the solid-phase Biot number was evaluated as

$$Bi_s = \frac{h_{eff} L_s}{L_s} \tag{10}$$

The resulting ranges were $Bi_{s,Al} = 0.007$–0.061 and $Bi_{s,Ag} = 0.004$–0.034. Since these values are below 0.1, thermal gradients across the characteristic metallic ligament thickness are expected to be small.

The phase response times were additionally estimated from

$$\tau_f \frac{\varepsilon(\rho C_p)_{nj}}{h_{eff} a_{sf}}, \quad \tau_s \frac{(1-\varepsilon)(\rho C_p)_s}{h_{eff} a_{sf}}, \tag{11}$$

and compared with the fluid residence time

$$\tau_{res} = \frac{\varepsilon V}{Q_v} \tag{12}$$

Across the investigated flow range, τ_{res} was approximately 0.21–1.13 s, whereas the estimated solid and fluid response times were approximately 0.23–1.9 s and 0.91–7.5 s, respectively. These results support rapid thermal redistribution within the highly conductive metallic skeleton but do not demonstrate perfect instantaneous equilibrium between the two phases. Accordingly, LTE is adopted here as a reduced-order homogenization approximation that enables a single-temperature PINN formulation. Potential solid–fluid temperature differences are acknowledged as a model limitation, and a two-temperature local thermal non-equilibrium (LTNE) formulation is recommended for future pore-scale investigations.

Under this assumption, the solid and fluid phases do not require separate temperature fields; instead, they are represented by a single local temperature, such that $T_f \approx T_s \approx T$. For the metallic TPMS structures and liquid nanofluid considered in this study, the high solid thermal conductivity and large solid–fluid interfacial area support this assumption. Therefore, both phases are treated as sharing a common temperature field, $T(x, y, z)$, which simplifies the porous-domain formulation to a single governing energy equation for the composite medium. Since the thermocouples are located along the plane $y = 0$, Equation (2) can be simplified by neglecting temperature variation in the y-direction at the measurement line. Therefore, the governing equation becomes:

$$\rho_{nf} C_{P,nf} u_p \frac{\partial T}{\partial x} = k_{eff} \left(\frac{\partial^2 T}{\partial x^2} + \frac{\partial^2 T}{\partial z^2} \right) \tag{13}$$

where T is the solid-nanofluid temperature and the effective thermal conductivity k_{eff}, given in Equation (4), represents the equivalent heat-conduction capability of the porous TPMS-nanofluid medium under the assumption of local thermal equilibrium. It combines the contribution of the solid TPMS material and the nanofluid occupying the pores.

This equation states that axial convective energy transport by the nanofluid is balanced by effective conduction or diffusion in the x-z plane. In residual form, the governing equation is written as

$$\mathcal{R}_{PDE} = \rho_{nf} C_{P,nf} u_p \frac{\partial T}{\partial x} - k_{eff} \left(\frac{\partial^2 T}{\partial x^2} + \frac{\partial^2 T}{\partial z^2} \right) \tag{14}$$

Note that $u_p = \varphi / \varepsilon WH$, where the term εWH represents the effective pore-flow cross-sectional area based on the porosity ε, W is the width of the TPMS and H is the height. During training, the PINN minimizes the mean squared value of this residual:

$$L_{PDE} = \frac{1}{N} \sum_{i=1}^{N} \mathcal{R}_{PDE,i}^2 \tag{15}$$

This forces the network to predict temperatures that not only match the experimental data, but also satisfy the governing heat transfer physics. At the bottom boundary, where the TPMS contacts the heated base, a constant heat flux boundary condition is applied:

$$-k_{eff}\frac{\partial T}{\partial z} = q'' \quad \text{at } z = 0 \tag{16}$$

which q'' is the imposed uniform heat flux and z denotes the outward normal direction. Convective heat removal by the nanofluid is governed implicitly through the energy balance between the inlet and outlet of the heat exchanger. The corresponding residual of the bottom heat flux boundary condition is

$$\mathcal{R}_{bottom} = -k_{eff}\frac{\partial T}{\partial z} - q'' \tag{17}$$

At the upper boundary of the TPMS region, an insulated condition is applied $\partial T/\partial z = 0$, and the top boundary residual is $\mathcal{R}_{top} = \partial T/\partial z$. At the outlet boundary, a zero streamwise temperature gradient condition is applied to represent a thermally developed outflow condition: applied $\partial T/\partial x = 0$ at $x = L$, and the outlet boundary residual is $\mathcal{R}_{outlet} = \partial T/\partial x$.

4.2. PINN Input-Output Structure

The complex coupling between TPMS geometry, nanofluid transport, and thermal behaviour motivates the use of a PINN as a surrogate modelling tool. The PINN is trained using both experimental thermocouple data and physics collocation points to predict the steady-state TPMS temperature as a function of operating conditions and nanofluid properties. In this approach, the convection–diffusion equation is not solved explicitly using a traditional numerical method such as CFD or finite element analysis. Instead, the neural network predicts the temperature field directly, while the governing energy equation is included as a physics-based constraint in the loss function. As a result, the model is trained to match the measured thermocouple temperatures while also satisfying the underlying heat transfer physics. During training, the PINN adjusts its weights so that the predicted temperature matches the experimental data and also satisfies the heat transfer physics. Each input point includes the spatial coordinates, flow rate, nanofluid concentration, solid thermal conductivity, nanofluid properties, pore velocity, and effective porous conductivity.

The input vector is defined as $X = [x, z, q, \dot{\varphi}, k_s, \rho_{nf}, C_{p,nf}, k_{nf}, \mu_{nf}, u_p, k_{eff}]$, and the output variable of the network is the temperature $Y = T$. The experimental training data are obtained from thermocouple measurements for aluminum and silver TPMS samples at different flow rates. The model is trained at the reference concentration of $\varphi_{ref} = 0.6\%$ vol. Each thermocouple measurement is paired with its corresponding input vector, allowing the neural network to learn the relationship between operating conditions, material properties, nanofluid properties, spatial location, and measured temperature. Before training, the input variables are normalized using the mean and standard deviation of each input feature $\widehat{X}_j = X_j - \mu x_j/\sigma_{X_j}$ and the output temperature is also normalized $\widehat{T} = T - \mu T/\sigma_T$. This normalization improves numerical stability, prevents variables with large magnitudes from dominating the training process, and allows the PINN to learn more efficiently from all input features.

The neural network is formulated as a feedforward network with eleven input features and one scalar output. The neural network is formulated as a fully connected feedforward neural network with eleven input features and one scalar output representing the TPMS interface temperature. The network consists of an input layer, four hidden layers, and

a single linear output layer. Each hidden layer contains 64 neurons and employs the hyperbolic tangent (tanh) activation function. The tanh function was selected because it is smooth, continuously differentiable, and well suited for automatic differentiation, allowing accurate evaluation of the first- and second-order derivatives required by the physics-informed loss function.

Prior to training, the network parameters were initialized using randomized weight values and zero-valued biases, providing a suitable starting point for gradient-based optimization. This initialization provides stable forward and backward propagation during training and improves convergence by reducing the risk of vanishing or exploding gradients. The network contains approximately 12,900 trainable parameters, including all weights and biases, providing sufficient representational capacity while maintaining computational efficiency.

4.3. Input Normalization and Output De-Normalization

To improve numerical stability and ensure balanced optimization during training, all continuous input variables were normalized before being supplied to the neural network. The axial position, x, volumetric flow rate, Q, and nanoparticle volume fraction, ϕ, were independently scaled to the interval [0, 1] using min–max normalization:

$$\widehat{X} = \frac{x - x_{min}}{x_{max} - x_{min}} \tag{18}$$

where X denotes the original variable, X~ is the normalized variable, and the subscripts "min" and "max" represent the minimum and maximum values of the corresponding variable in the training dataset. The TPMS interface temperature was normalized using the same procedure:

$$\widehat{T} = \frac{T - T_{min}}{T_{max} - T_{min}} \tag{19}$$

The normalization parameters obtained from the training dataset were consistently applied to all experimental data, collocation points, and boundary condition points, ensuring that the data loss, governing-equation residual, and boundary condition residual were evaluated within the same normalized domain throughout the training process. Because the present study considers only aluminum TPMS specimens during network training, no categorical input variables were included and no material encoding was required. After training, the normalized network output was transformed back to the physical temperature using the inverse min–max transformation:

$$T = \widehat{T}(T_{max} - T_{min}) + T_{min} \tag{20}$$

The reconstructed temperature field was then used to determine the mean TPMS wall temperature, from which the effective heat transfer coefficient and Nusselt number were subsequently evaluated using the energy balance formulation.

If the neural network is denoted by N_θ, where θ represents the trainable weights and biases, the normalized network prediction is $\widehat{T}_{pred} = N_\theta(\widehat{X})$ and the corresponding physical temperature prediction is given by $T_{pred} = N_\theta(\widehat{X})\sigma_T + \mu_T$.

The prediction input vector is then constructed as

$$X_{pred} = \left[x, z, q, \varphi, k_s, \rho_{nf}(\varphi), C_{p,nf}(\varphi), k_{nf}(\varphi), \mu_{nf}(\varphi), u_p, k_{eff}(\varphi)\right] \tag{21}$$

The predicted temperature field is calculated as

$$T(x, z, q, \varphi, k_s) = N_\theta(\widehat{X})\sigma_T + \mu_T \tag{22}$$

The one-dimensional thermocouple temperature profile is obtained by evaluating the trained model at the thermocouple measurement locations.

4.4. Physics-Informed Loss Function

The training objective of the PINN is constructed as a composite loss function that enforces agreement with experimental data while simultaneously satisfying physical constraints. The total training loss consists of the experimental data loss, the governing-equation residual loss, and the boundary condition losses. The supervised data loss is calculated based on Equation (15) as

$$\mathcal{L}_{data} = \frac{1}{N_d}\sum_{i=1}^{N_d}\left(\widehat{T}_{pred,i}(p_i, q_i, \varphi_i, \ldots) - T_{s,i}^{exp}(p_i, q_i, \varphi_i, \ldots)\right)^2 \tag{23}$$

Similarly, the PDE residual loss is calculated and the bottom heat flux boundary loss as

$$\mathcal{L}_{PED} = \frac{1}{N_f}\sum_{i=1}^{N_f}\left(\frac{\mathcal{R}_{PDE,i}}{q''}\right)^2 \tag{24}$$

The remaining boundary condition losses are formulated using the same mean-squared residual approach. The bottom heat flux boundary loss is obtained from the heat flux residual, while the outlet and top insulated-boundary losses are calculated using the corresponding outlet and insulation residuals, respectively, as expressed in Equation (23).

$$\mathcal{L}_{outlet} = \frac{1}{N_o}\sum_{i=1}^{N_o}(\mathcal{R}_{outlet,i})^2 \tag{25}$$

The total loss function minimized during training is

$$\mathcal{L}_{total} = \lambda_{data}\mathcal{L}_{data} + \lambda_{PDE}\mathcal{L}_{PDE} + \lambda_{outlet}\mathcal{L}_{outlet} + \lambda_{bottom}\mathcal{L}_{bottom} + \lambda_{top}\mathcal{L}_{top} \tag{26}$$

here $\lambda_{data} = 100$ controls how strongly the model fits the experimental thermocouple data; the model gives high priority to matching the measured temperatures. $\lambda_{PDE} = 0.005$ which controls the importance of satisfying the governing heat transfer equation. This means the PDE residual is included, but it is not allowed to dominate the experimental data fitting. The boundary condition weights are $\lambda_{outlet} = \lambda_{bottom} = \lambda_{top} = 0.05$ and control how strongly the model enforces the outlet, bottom heat flux, and top insulated boundary conditions. Note that these coefficients are not universal physical constants and not values from literature. They are hyperparameters chosen in the PINN model to balance data fitting and physics constraints.

It should be emphasized that the PINN predicts only the TPMS temperature field. The effective heat transfer coefficient and Nusselt number are not direct outputs of the neural network. Instead, they are calculated from the PINN-predicted temperatures using the energy balance formulation. Likewise, the Reynolds–Prandtl-based concentration scaling model is used solely to predict the temperature field at nanoparticle concentrations beyond the experimental reference condition and does not contribute directly to the evaluation of the heat transfer coefficient or Nusselt number.

4.5. Training Procedure and Collocation Point Selection

The network parameters were optimized using the Adam optimization algorithm [40] with a fixed learning rate of 1×10^{-3} and the default exponential decay coefficients $\beta_1 = 0.9$ and $\beta_2 = 0.999$. Training was performed for 7000 epochs using a fixed set of collocation and boundary points. During each epoch, automatic differentiation was employed to evaluate

the gradients of the composite loss function with respect to all trainable parameters, and the resulting gradients were back-propagated to update the network weights and biases. A fixed random seed was used throughout training to ensure reproducibility, while the individual loss components were monitored every 500 epochs to verify stable convergence.

The PINN was trained using experimental temperature measurements obtained for pure water and a reference nanofluid concentration of $\varphi = 0.6\%$. The experimental dataset consisted of seven thermocouple measurements distributed along the TPMS axial direction for five volumetric flow rates, resulting in a total of 35 temperature observations for each working fluid. These experimental measurements served as the supervised training data, enabling the network to reconstruct the TPMS temperature field at the reference operating conditions. Temperature predictions at higher nanoparticle concentrations were subsequently obtained using the correlation-based concentration scaling the developed PINN model.

To enforce the governing heat transfer physics, a set of collocation points was uniformly distributed throughout the one-dimensional computational domain along the TPMS axial direction and over the investigated range of flow rates. Unlike the experimental measurements, the collocation points did not require temperature data and were used exclusively to evaluate the residual of the governing convection–diffusion equation within the physics-informed loss function. The number of collocation points was selected to be substantially larger than the number of experimental observations to ensure adequate enforcement of the governing physical constraints throughout the solution domain.

Owing to the limited size of the experimental dataset, all measured temperature data were used for network training, while the physics residual evaluated at the collocation points acted as an intrinsic regularization mechanism that reduced the risk of overfitting. Consequently, a separate validation or testing dataset was not employed. Instead, the predictive capability of the trained PINN was assessed by comparing the reconstructed temperature profiles with the experimental measurements and by evaluating the corresponding heat transfer coefficient and Nusselt number derived from the PINN-predicted temperature field.

Training convergence was assessed by monitoring the total loss together with its individual data, PDE, and boundary condition components throughout the optimization process. The results show that all loss components decrease rapidly during the initial training stage and gradually approach stable plateaus as the training progresses. During the final stage of training, no appreciable reduction in the loss was observed, indicating that the network parameters had converged and that additional training epochs would provide negligible improvement in the predicted temperature field. Based on this convergence behaviour, 7000 training epochs were considered sufficient for the present study.

4.6. Computational Cost and Implementation

The proposed PINN was implemented in MATLAB using the Deep Learning Toolbox. Network training was performed on a workstation equipped with an AMD Ryzen 7 9700F 8-Core Processor, 64.0 GB RAM, and an 8 GB GeForce RTX5060 graphics card (Canada Computers, Richmond Hill, ON, Canada). The complete training process required approximately (training time) to reach convergence after 7000 epochs. The peak memory usage during training was approximately 30–40% of the total memory. Once trained, the PINN required about 40 to 80 min to predict the complete temperature field for a new combination of flow rate and nanoparticle concentration.

Unlike conventional CFD simulations, which require solving the governing equations for each new operating condition, the trained PINN performs only a forward evaluation of the neural network during inference. Consequently, the computational cost of generating

new temperature predictions is negligible compared with the one-time training cost. This characteristic makes the proposed approach particularly suitable for rapid parametric studies, optimization, and real-time engineering applications involving TPMS heat exchangers.

4.7. Physics-Based Concentration Scaling Model

The experimental data available for training were limited to pure water and the reference nanofluid concentration $\varphi_{ref} = 0.6\%$. Consequently, the PINN was trained to reconstruct the TPMS temperature field only at these experimentally measured operating conditions. To extend the predictions to other nanoparticle concentrations without requiring additional experiments, a physics-based concentration scaling model was employed.

The scaling model is based on the concentration-dependent changes in the Reynolds number, Prandtl number, and effective thermal conductivity, whose definitions and thermophysical property models are presented in the next section. The corresponding Nusselt number ratio between an arbitrary concentration φ and the reference concentration φ_{ref} is expressed as

$$\frac{Nu(\varphi)}{Nu(\varphi_{ref})} = \left(\frac{Re(\varphi)}{Re(\varphi_{ref})}\right)^{a}\left(\frac{Pr(\varphi)}{Pr(\varphi_{ref})}\right)^{b}\left(\frac{k_{nf}(\varphi)}{k_{nf}(\varphi_{ref})}\right)^{c} \tag{27}$$

where $a = 0.3$, $b = 1/3$, and $c = 0.5$. Since the convective heat transfer coefficient satisfies $h \propto Nuk_{nf}$, the PINN-predicted reference temperature field is corrected according to

$$T_s(Q, x, \varphi) = T_\infty + \left[T_{PINN}\left(Q, x, \varphi_{ref}\right) - T_\infty\right]\left(\frac{Re_{ref}}{Re}\right)^{a}\left(\frac{Pr_{ref}}{Pr}\right)^{b}\left(\frac{k_{ref}(\varphi)}{k}\right)^{c+1} \tag{28}$$

Accordingly, the PINN reconstructs the reference temperature field directly from the experimental measurements, while the concentration scaling model modifies this field to account for the concentration-dependent variation in the nanofluid transport properties. This hybrid strategy enables predictions over the investigated concentration range without requiring additional experimental measurements for every nanoparticle concentration.

4.8. Heat Transfer Performance Evaluation

The trained PINN reconstructs the spatial temperature distribution within the TPMS gyroid heat exchanger for the experimentally measured reference nanofluid concentration. The predicted temperature field is first used to determine the mean TPMS wall temperature, from which the effective heat transfer coefficient and Nusselt number are evaluated using the energy balance formulation presented in Equations (23)–(26). Thus, the thermal performance metrics are derived directly from the PINN-predicted temperature field rather than from empirical heat transfer correlations. The Reynolds–Prandtl concentration scaling introduced in this section is employed only to extend the PINN predictions to nanoparticle concentrations beyond the experimental dataset by accounting for the corresponding changes in nanofluid thermophysical properties [48].

The Reynolds number was calculated as

$$R_e = \frac{\rho_{nf} u_p D_h}{\mu_{nj}} \tag{29}$$

where ρ_{nf} is the nanofluid density, D_h is the hydraulic diameter used is $D_h = 0.01$ m, and μ_{nj} is the nanofluid dynamic viscosity. The Prandtl number was calculated as:

$$P_r = \frac{\mu_{nf} C_{p,nf}}{k_{nj}} \tag{30}$$

where $C_{p,nf}$ is the nanofluid specific heat capacity and k_{nj} is the nanofluid thermal conductivity. In principle, the local interfacial heat flux may be evaluated from the PINN-predicted temperature field using Fourier's law $q'' = -k_s(\partial T_s/\partial n)_{int}$. However, the thermocouple measurements used to train the present PINN are distributed primarily in the axial direction and are positioned approximately 1 mm below the TPMS–fluid interface. The interface-normal temperature gradient is therefore not directly measured and is insufficiently constrained for a reliable gradient-based evaluation of the local heat flux. Because numerical differentiation may amplify uncertainties in a sparsely reconstructed temperature field, the present study evaluates the effective heat transfer coefficient using an overall energy balance. The PINN-predicted temperature field supplies the mean wall temperature, whereas the measured fluid temperature rise determines the total heat transfer rate.

The PINN contributes directly to the Nusselt number evaluation through its prediction of the mean wall temperature, while the total heat transfer rate is obtained independently from the fluid-side energy balance.

The base Nusselt number, Nu_{base}, was calculated using a conventional forced-convection correlation based on the Reynolds and Prandtl numbers. It represents the basic convective heat transfer behaviour of the flow before applying any additional correction for nanoparticle concentration.

$$Nu_{base} = C_{Nu} Re^{mNu} P^{nNu} \tag{31}$$

In this study, Nu_{base} used as a reference value to include the effects of flow intensity, viscosity, thermal diffusivity, and pore-scale convection inside the TPMS channels. The effective Nusselt number was then obtained by applying a concentration-dependent enhancement factor, allowing the model to account for the additional heat transfer improvement caused by Al_2O_3 nanoparticle addition [49,50]. The constants used in the model are: $C_{Nu} = 1.8$, $mNu = 0.42$ and $nNu = 0.33$. Thus, the effective heat transfer coefficient is calculated as

$$h_{eff} = \frac{Nu_{base} k_{nf}}{D_h} \tag{32}$$

Since the TPMS solid has much higher thermal conductivity than the nanofluid, changes in k_{nf} have little influence on k_{eff}. The Nusselt correction allows the model to include convective enhancement associated with nanoparticle concentration, Reynolds number, Prandtl number, and nanofluid thermal conductivity. The effective heat-removal is calculated as

$$\dot{Q}_{rem} = h_{eff} A_s \max(T_{mean} - T_{in}, 0) \tag{33}$$

where $A_s = 15.524 \times 10^{-4}$ m^2 is the TPMS heat transfer area, and $T_{mean} = \frac{1}{N_{tc}} \sum_{i=1}^{N} T_{tc,i}$ is the mean temperature. This heat-removal index is used as a comparative performance metric to evaluate the influence of flow rate and nanofluid concentration on the effective heat-removal capability of the TPMS structure.

For three-dimensional visualization, the STL file of the gyroid TPMS structure is imported into the model. The STL vertex coordinates are mapped into the physical domain. The physical streamwise and the physical vertical coordinates are calculated as

$$x_{phys} = L \frac{x_{STL} - x_{min}}{x_{max} - x_{min}} \text{ and } z_{phys} = H \frac{z_{STL} - z_{min}}{z_{max} - z_{min}} \tag{34}$$

The trained PINN is then evaluated at each STL vertex $T_{STL} = T(x_{phys}, z_{phys}, q, \varphi, k_s)$. The predicted temperature values are assigned to the STL vertices as colour data, producing a three-dimensional thermal visualization of the TPMS. This visualization allows the spatial temperature distribution to be interpreted directly on the complex gyroid geometry.

4.9. Model Validation and Accuracy Assessment

The validation strategy adopted in the present study builds on the framework previously established for PINN-based thermal prediction in porous TPMS metals [29]. In that earlier work, the model was first verified using published digitized temperature-distance data from Islam et al. [51]. Specifically, temperature profiles at selected time steps were digitized and used to test whether the implemented neural network framework could reproduce the reference thermal response. The predicted profile showed strong agreement with the published data, confirming the correctness of the inverse-model implementation and the stability of the training procedure.

The previous work was then further validated using experimental measurements from aluminum and silver TPMS gyroid samples tested under identical heating and flow conditions. The PINN-predicted temperature fields were compared directly with the measured thermocouple temperatures across all flow rates and axial locations. The use of two materials with different thermal conductivities provided independent thermal responses and helped confirm that the model could capture both material-dependent and flow-dependent temperature variations.

Based on this previously validated framework, the present nanofluid study applies the same validation philosophy to the Al_2O_3–*water* TPMS heat-exchanger problem. In the current model, the PINN predictions are evaluated against experimental thermocouple measurements for pure water and nanofluid cases using both aluminum and silver TPMS samples. This ensures that the developed model is assessed not only for numerical accuracy, but also for physical consistency across different materials, flow rates, and working-fluid conditions.

The accuracy of the developed PINN model was evaluated by comparing the predicted thermocouple temperatures with the corresponding experimental thermocouple measurements. After the training process was completed, the normalized output of the neural network was converted back to the physical temperature scale using the de-normalization relation:

$$T_{pred} = \widehat{T}_{pred}\sigma_T + \mu_T \tag{35}$$

where T_{pred} is the predicted temperature, $\widehat{T}_{pred}$ is the normalized output of the neural network, σ_T is the standard deviation of the training temperature data, and μ_T is the mean value of the training temperature data.

The predicted temperatures were compared with the experimental temperatures at all thermocouple locations and for all tested flow rates. The model accuracy was quantified using the RMSE, MAPE, and coefficient of determination. RMSE and MAPE were used to evaluate the prediction accuracy of the PINN model. The RMSE was used to quantify the average temperature prediction error in degrees Celsius and is expressed as

$$RMSE = \sqrt{\frac{1}{N}\sum_{i=1}^{N}\left(T_{pred,i} - T_{exp,i}\right)^2} \tag{36}$$

where N is the total number of thermocouple data points, $T_{pred,i}$ is the predicted temperature at the i-th point, and $T_{exp,i}$ is the corresponding experimental temperature. The MAPE is used to express the average percentage deviation between the predicted and experimental values. It is calculated as

$$MAPE = \frac{100}{N}\sum_{i=1}^{N}\left|\frac{T_{pred,i} - T_{exp,i}}{T_{exp,i}}\right| \tag{37}$$

The coefficient of determination was used to evaluate how well the predicted temperatures follow the variation in the experimental data. It is defined as

$$\mathcal{R}^2 = 1 - \frac{\sum_{i=1}^{N}(T_{pred,i} - T_{exp,i})^2}{\sum_{i=1}^{N}(T_{exp,i} - \overline{T}_{exp,i})^2} \tag{38}$$

where $\overline{T}_{exp,i}$ is the mean value of the experimental temperatures. Values of $\mathcal{R}^2$ close to unity indicate that the model captures most of the physical variability present in the measurements.

The initial validation results obtained from the trained PINN showed small error values, indicating that the trained PINN reproduced the experimental thermocouple temperatures with high accuracy. The overall RMSE value shows that the magnitude of the prediction error was very low, while the MAE value confirms that the average absolute difference between the predicted and measured temperatures was minimal. The statistical performance of the model was also evaluated separately for the aluminum and silver TPMS samples. The material-specific validation results are summarized in Table 3.

Table 3. Statistical performance metrics of the PINN predictions for aluminum and silver, including root mean square error (RMSE), mean absolute percentage error (MAPE), and coefficient of determination R^2 evaluated across all flow rates and streamwise locations.

Material	RMSE (°C)	MAPE (%)	Coefficient of Determination (R^2)	Agreement Assessment
Aluminum φ = 0.6% vol	0.0148	0.0459	0.99998	Excellent
Silver φ = 0.6% vol	0.0393	0.1469	0.99971	Excellent
Aluminum φ = 0 (water)	0.0230	0.0689	0.99992	Excellent
Silver φ = 0 (water)	0.0292	0.0979	0.99987	Excellent
Overall	0.0266	0.0899	0.99994	Excellent

Although the error values for silver were slightly higher than those for aluminum, the prediction accuracy remained very high, as confirmed by the coefficient of determination close to unity.

The PINN was trained using the experimental thermocouple measurements at the reference nanofluid concentration to reconstruct the TPMS temperature field while satisfying the governing heat transfer equations. The predicted temperature field is subsequently used to determine the mean TPMS wall temperature, from which the effective heat transfer coefficient and Nusselt number are calculated using an overall energy balance. For nanoparticle concentrations beyond the experimental reference case, a Reynolds–Prandtl-based scaling relation is introduced only to account for the concentration dependence of the nanofluid thermophysical properties and to extend the PINN predictions. Consequently, the empirical correlation supplements the PINN during extrapolation rather than replacing the physics-informed temperature prediction.

4.10. LTE–LTNE Sensitivity Analysis

To assess the influence of the local thermal equilibrium assumption, a sensitivity analysis was performed by comparing the LTE model with an LTNE formulation that treats the solid TPMS skeleton and nanofluid as separate temperature fields. The aluminum TPMS case at the highest investigated volumetric flow rate, $Q = 19.85\ \mathrm{cm}^3/\mathrm{s}$, and nanoparticle volume fraction, $\varphi = 25\%$, was selected as a conservative test condition because the high flow rate produces the shortest fluid residence time and is therefore more likely to generate interphase thermal disequilibrium.

Under LTNE conditions, the volume-averaged solid and fluid energy equations are written as

$$\nabla\cdot[(1-\varepsilon)k_s\nabla T_s - h_{sf}a_{sf}(T_s - T_f) = 0 \quad (39)$$

$$\varepsilon\rho_{nf}C_{p,nf}u\cdot\nabla T_f = \varepsilon k_{nf}\nabla^2 T_f + h_s a_{sf}(T_s - T_f) \quad (40)$$

The LTNE results were compared with those from the single-temperature LTE model using the mean TPMS temperature, maximum temperature, effective heat transfer coefficient, Nusselt number, and maximum phase temperature difference. The relative deviation of a predicted quantity Y was evaluated as

$$\delta_Y = \frac{|Y_{LET} - Y_{LTNE}|}{Y_{LTNE}} \times 100 \quad (41)$$

The LTE and LTNE temperature profiles were compared at the seven thermocouple positions, as shown in Figure 3. The LTE temperature, LTNE solid temperature, and LTNE fluid temperature follow similar axial trends. The temperatures remain nearly constant in the upstream region and subsequently increase toward the downstream portion of the TPMS structure. The LTE model predicts slightly higher temperatures than the LTNE solid phase, while the LTNE fluid phase exhibits the lowest temperature. Nevertheless, the three profiles remain closely spaced and preserve the same spatial variation, indicating that the LTE approximation captures the dominant thermal behaviour of the TPMS heat exchanger.

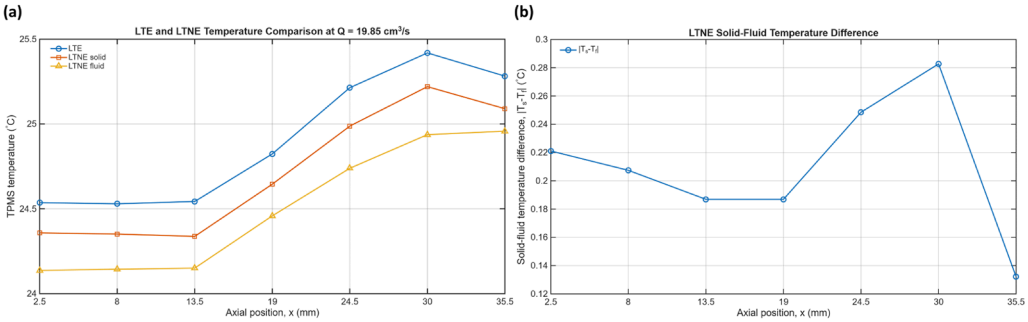

Figure 3. LTE-LTNE sensitivity analysis at Q = 19.85 cm^3/s: (**a**) comparison of the LTE temperature profile with the LTNE solid- and fluid-phase temperature profiles along the seven thermocouple positions; (**b**) absolute solid–fluid phase temperature difference.

The local LTNE solid–fluid temperature difference, $|T_s - T_f|$, ranges from approximately 0.130 to 0.28 °C across the thermocouple positions. The maximum phase temperature difference occurs near $x = 30$ mm, whereas the minimum occurs at the final thermocouple position. These relatively small temperature differences indicate strong thermal coupling between the metallic TPMS skeleton and the nanofluid. Therefore, the LTE formulation provides a reasonable reduced-order approximation for the investigated operating condition, although small local solid–fluid temperature differences remain and are explicitly acknowledged.

The small interphase temperature differences indicate strong solid–fluid thermal coupling and support the use of the LTE approximation for the investigated condition. Conventional prediction of heat transfer in TPMS heat exchangers is typically performed using three-dimensional computational fluid dynamics (CFD) solvers, such as ANSYS Fluent or COMSOL Multiphysics, based on finite volume or finite element formulations. These approaches require the complete solution of the governing conservation equations for each combination of flow rate, nanoparticle concentration, and material properties. Because TPMS geometries contain highly interconnected porous channels, accurate simulations generally require fine computational meshes and significant computational resources,

making large parametric studies computationally expensive. In contrast, the proposed PINN reconstructs the temperature field directly from the trained model. Although the initial training stage requires additional computational effort, prediction of new operating conditions is completed within seconds, providing a substantial reduction in computational cost compared with repeatedly solving the governing equations using conventional CFD methods.

4.11. Limitations and Assumptions

The model assumes steady-state heat transfer, constant thermophysical properties at each nanoparticle concentration, uniform heat flux at the TPMS-base interface, and an effective porous-medium representation of the TPMS domain. The nanofluid is treated using a single-phase effective-property approach, where the nanoparticle and base fluid are assumed to move with the same average velocity. The empirical concentration enhancement factor is used only to represent the expected convective improvement with increasing Al_2O_3 volume fraction and should be interpreted as a calibrated heat transfer correction rather than a direct experimental measurement at each concentration.

The LTE formulation assumes a common local temperature for the TPMS skeleton and nanofluid. Although the calculated solid-phase Biot numbers are below 0.1, the estimated phase response times are not uniformly much smaller than the fluid residence time. Therefore, possible local solid–fluid temperature differences cannot be excluded, particularly at the highest flow rates and near the heated interface. The resulting temperature field and heat transfer coefficients should be interpreted as effective volume-averaged quantities. Future work should employ an LTNE formulation with separate solid and fluid energy equations coupled through a pore-scale interstitial heat transfer coefficient.

Another limitation of the present study is that the PINN was trained and experimentally validated using pure water and a single reference nanofluid concentration $\varphi_{ref} = 0.6\%$. Predictions at higher nanoparticle concentrations were obtained using the proposed physics-based concentration scaling model and were not directly validated against independent experimental measurements. Future work will include additional experiments at intermediate and higher nanoparticle concentrations to further assess the extrapolation capability and robustness of the proposed framework.

5. Results and Discussion

The results presented in this section evaluate the performance of the proposed PINN for predicting the thermal behaviour of nanofluid flow through TPMS gyroid heat exchangers. The PINN was developed to reconstruct the temperature response of the system by combining experimental temperature data with the governing heat transfer physics. This approach allows the model to preserve the physical structure of the convection–diffusion problem while providing continuous temperature predictions across different flow rates, materials, and nanoparticle concentrations.

In the present framework, the PINN is used as the primary predictor of the TPMS temperature field. The predicted temperatures are subsequently used to evaluate the mean TPMS wall temperature, from which the effective heat transfer coefficient is obtained through an energy balance. The corresponding Nusselt number is then calculated using the predicted heat transfer coefficient and the concentration-dependent nanofluid thermal conductivity. The empirical Reynolds–Prandtl scaling relation is employed only to extend the PINN solution from the experimentally measured reference concentration to additional nanoparticle concentrations.

5.1. PINN Prediction and Training Performance Accuracy

The discussion first examines the prediction accuracy and training behaviour of the PINN, as shown in Figure 4a,b. Figure 4a evaluates the agreement between the experimental and PINN-predicted temperatures using a parity plot, while Figure 4b presents the evolution of the total, data, PDE, and boundary condition loss components during training. These results provide the basis for assessing whether the trained PINN is sufficiently accurate and stable before using it for further heat transfer analysis, including temperature-field reconstruction, convective heat transfer coefficient estimation, and Nusselt number evaluation. Figure 4a compares the experimental temperatures with the PINN-predicted temperatures for pure water $\varphi = 0$ and nanofluid $\varphi = 0.6\%$ vol using aluminum and silver TPMS samples. The data points are closely aligned with the diagonal reference line, indicating strong agreement between the measured and predicted values. This confirms that the PINN accurately reproduces the experimental thermal response over the investigated temperature range without noticeable over-prediction or under-prediction. The agreement observed for both aluminum and silver samples also shows that the model can represent different thermal-conductivity conditions. This suggests that the embedded heat transfer physics and material-property inputs help the PINN generalize across different TPMS thermal responses, supporting its use as a surrogate model for temperature-field reconstruction.

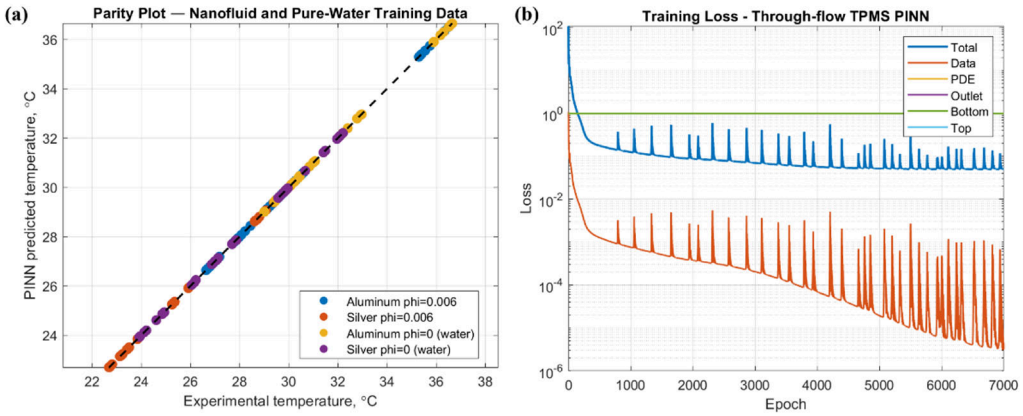

Figure 4. Performance evaluation of the proposed through-flow TPMS PINN model: (**a**) parity plot comparing experimental and PINN-predicted temperatures for pure water (ϕ = 0) and nanofluid (ϕ = 0.006) cases using aluminum and silver TPMS samples; (**b**) training-loss history showing the evolution of the total, data, PDE, and boundary condition loss components over 7000 epochs.

Figure 4b shows the training-loss history of the through-flow TPMS PINN over 7000 epochs. The total loss decreases rapidly at the beginning of training and then gradually stabilizes, indicating that the model first captures the dominant thermal behaviour and then refines the remaining errors. The data loss decreases by several orders of magnitude, demonstrating that the network fits the experimental temperature data with high accuracy. Although the total loss remains higher than the data loss, this is mainly due to the contribution of the physics-informed and boundary condition terms. The repeated spikes in the loss curves are likely related to optimizer updates or adaptive sampling, but they do not interrupt the overall convergence trend. Therefore, Figure 4 confirms that the proposed PINN provides accurate predictions while maintaining stable training performance, making it suitable for subsequent heat transfer and Nusselt number analysis.

Additionally, as shown in Figure 4b, the boundary condition loss rapidly converges during the initial training stage and subsequently remains nearly constant because the prescribed boundary conditions are relatively simple and are satisfied early in the optimization process. In contrast, the data loss and total loss continue to exhibit small

fluctuations as the optimizer simultaneously minimizes the experimental data mismatch and the governing equation residual. These oscillations are characteristic of multi-objective optimization in physics-informed neural networks and gradually diminish as the network approaches convergence.

Figure 5 further compares the PINN-predicted thermocouple temperature profiles with the experimental measurements for pure water $\varphi = 0$ and nanofluid $\varphi = 0.6\%$ vol for one of the investigated flow rate of $Q = 7.786\ \mathrm{cm}^3/\mathrm{s}$. The comparison is shown for both aluminum and silver TPMS samples. For all cases, the PINN predictions closely follow the experimental temperature profiles along the thermocouple positions, confirming that the model can accurately capture the spatial temperature variation inside the TPMS heat exchanger. For the aluminum sample, Figure 5a shows that the PINN reproduces the increasing downstream temperature trend for both pure water and nanofluid. Similarly, for the silver sample, Figure 5b shows excellent agreement between the predicted and measured profiles, including the relatively flatter temperature distribution caused by the higher thermal conductivity of silver.

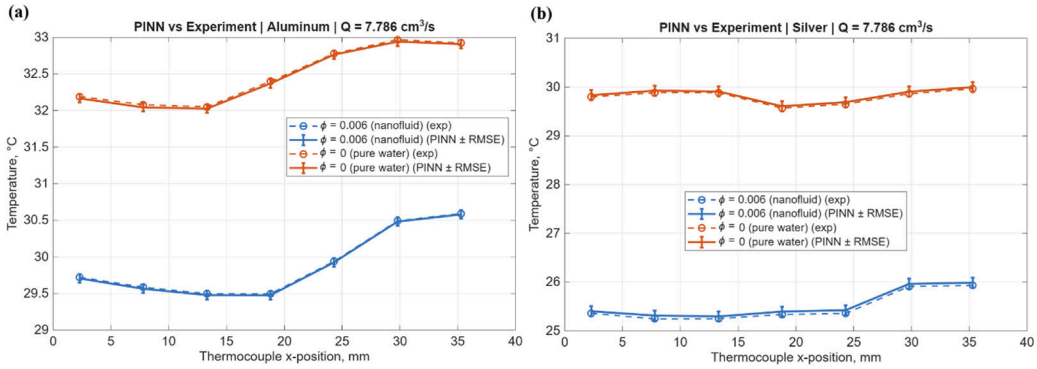

Figure 5. Comparison between experimental and PINN-predicted thermocouple temperature profiles at $Q = 7.86\ \mathrm{cm}^2/\mathrm{s}$ for pure water $\varphi = 0$ and nanofluid $\varphi = 0.6\%$: (**a**) aluminum TPMS sample and (**b**) silver TPMS sample. Error bars represent the RMSE-based prediction uncertainty and are enlarged by 3% for improved visibility.

The close overlap between the experimental data and PINN predictions demonstrates that the model can predict both the baseline pure-water case and the $\varphi = 0.6\%$ vol nanofluid case with very high accuracy.

The error bars represent the prediction uncertainty based on the RMSE and were enlarged by 3% to improve visibility in the graphs. Even with the enlarged error bars, the predicted profiles remain very close to the experimental measurements, confirming the robustness of the PINN model. This agreement supports the use of the trained PINN for reconstructing temperature fields and for subsequent heat transfer coefficient and Nusselt number calculations.

5.2. Effect of Nanoparticle Concentration on Thermocouple Temperature Profiles

Figure 6 shows the PINN-predicted temperature profiles along the thermocouple positions for the aluminum and silver TPMS samples at a fixed flow rate of $Q = 7.786\ \mathrm{cm}^3/\mathrm{s}$ and $z = -1$ mm. For both materials, the predicted temperature decreases as the nanoparticle volume concentration increases. The highest temperatures are observed for pure water $\varphi = 0$, while the lowest temperatures occur at the highest concentration $\varphi = 2.5\%$ vol.

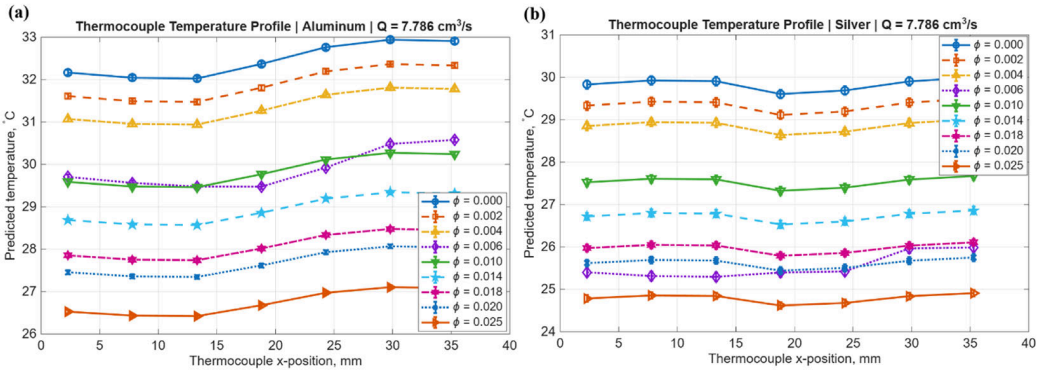

Figure 6. PINN-predicted thermocouple temperature profiles along the streamwise x-position at $Q = 7.786$ cm^3/s and z = −1 mm for different nanoparticle volume fractions (φ = 0–0.025): (**a**) aluminum TPMS sample and (**b**) silver TPMS sample.

This confirms that adding nanoparticles improves the effective thermal transport of the working fluid and enhances heat removal from the TPMS structure. For the aluminum sample, Figure 6a shows a gradual increase in temperature along the thermocouple positions, especially toward the downstream region.

This indicates that heat accumulates as the fluid progresses through the TPMS channels. However, increasing the nanoparticle concentration shifts the entire temperature profile downward, showing that the nanofluid reduces the TPMS temperature across all axial locations. The reduction becomes more pronounced at higher concentrations because the enhanced effective thermal conductivity strengthens heat diffusion from the solid structure to the flowing fluid.

For the silver sample, Figure 6b shows lower overall temperatures compared with aluminum. This behaviour is consistent with the higher thermal conductivity of silver, which promotes faster heat spreading and reduces localized thermal accumulation.

As a result, the silver TPMS sample exhibits a more uniform temperature distribution along the thermocouple positions. To quantify the cooling enhancement, the relative percentage temperature reduction between pure water $\varphi = 0$ and the highest nanofluid concentration $\varphi = 2.5$ vol was calculated using

$$Temperature\ Reduction = \frac{T_{\varphi=0} - T_{\varphi=0.025}}{T_{\varphi=0}} \times 100\% \quad (42)$$

Based on this calculation, the predicted temperature reduction ranges from approximately 17.5% to 18.5% when the nanoparticle concentration increases from $\varphi = 0$ to $\varphi = 2.5$% vol. This quantitative reduction confirms that the use of Al_2O_3–*water* anofluid provides a meaningful cooling improvement compared with pure water. The reduction is observed across the thermocouple locations, indicating that the enhancement is not localized at a single point but occurs throughout the measured region of the TPMS heat exchanger. This behaviour is also observed at the other investigated flow rates, as shown in Figures 7 and 8. For the aluminum TPMS sample, the predicted temperature profiles consistently decrease as the nanoparticle concentration increases.

The same trend is observed for the silver sample, confirming that the cooling enhancement is not limited to one material or one operating condition. The profiles also show that increasing the flow rate generally lowers the predicted temperature level. At higher flow rates, stronger forced convection improves heat extraction from the TPMS structure, resulting in lower surface temperatures.

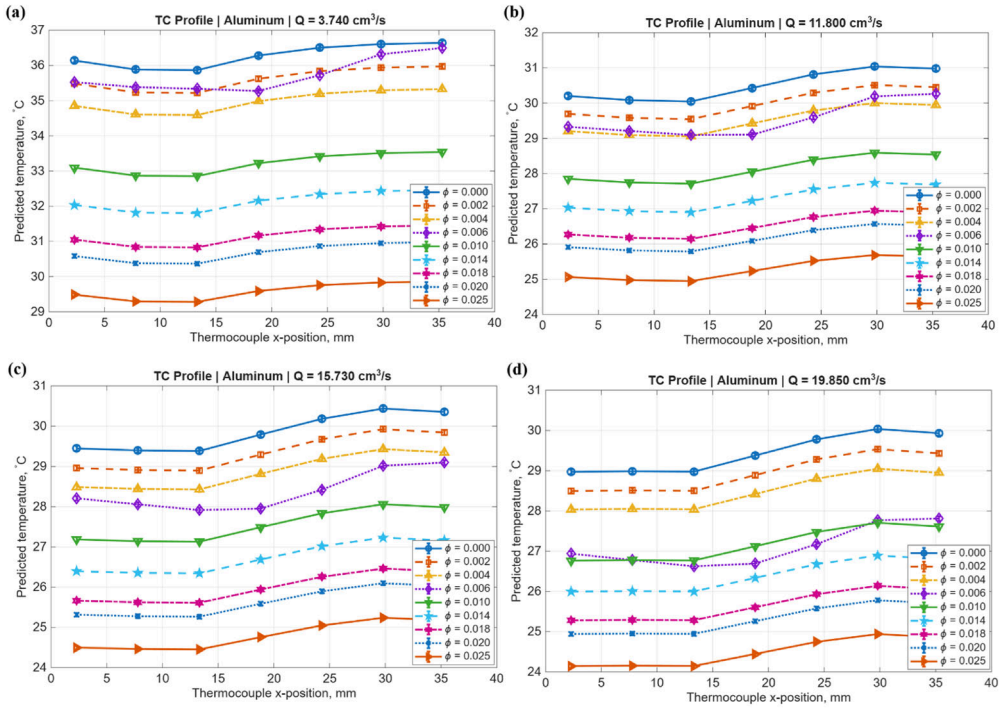

Figure 7. PINN-predicted thermocouple temperature profiles for the aluminum TPMS sample at different nanoparticle volume fractions (φ = 0–0.025) and volumetric flow rates: (**a**) Q = 3.74 cm^3/s (**b**) Q = 11.8 cm^3/s (**c**) Q = 15.73 cm^3/s (**d**) Q = 19.85 cm^3/s.

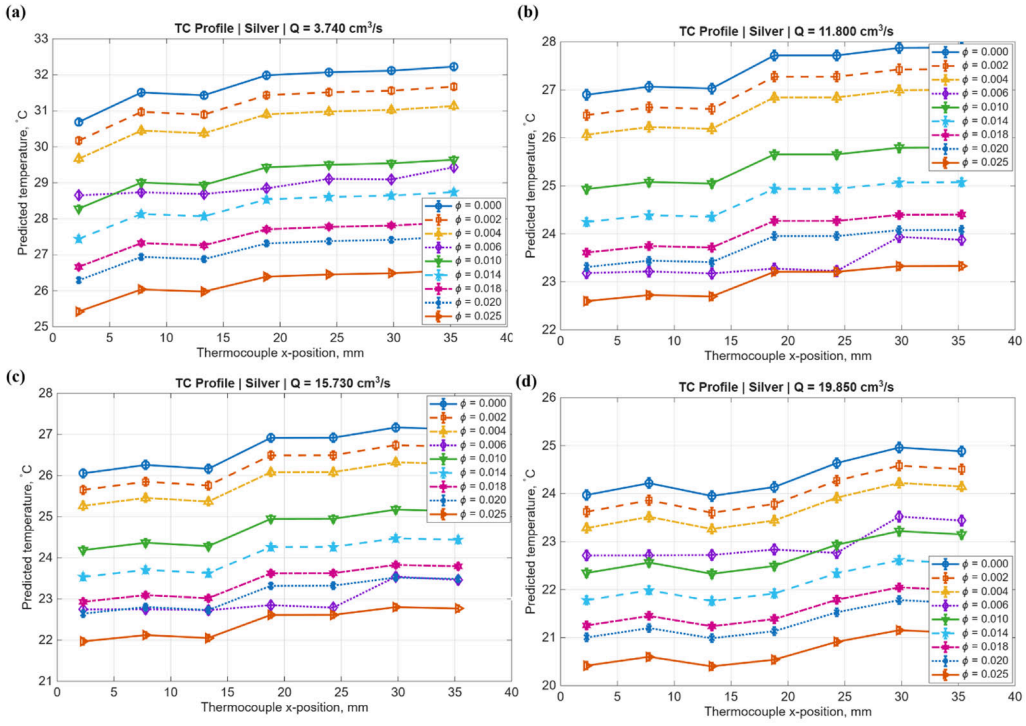

Figure 8. PINN-predicted thermocouple temperature profiles for the silver TPMS sample at different nanoparticle volume fractions (φ = 0–0.025) and volumetric flow rates: (**a**) $Q = 3.74$ cm^3/s (**b**) $Q = 11.8$ cm^3/s (**c**) $Q = 15.73$ cm^3/s (**d**) $Q = 19.85$ cm^3/s.

Although the magnitude of the temperature reduction varies with thermocouple position, nanoparticle concentration, and material type, the overall trend remains physically consistent: higher flow rates and higher nanoparticle concentrations both contribute to improved thermal performance.

Consequently, Figures 6–8 demonstrate that both material conductivity and nanoparticle concentration strongly influence the predicted thermal response. Increasing the nanoparticle concentration φ, improves cooling performance by reducing the predicted thermocouple temperatures, while the silver structure provides lower and more uniform temperatures than aluminum.

The calculated 17.5% to 18.5% temperature reduction further supports the effectiveness of nanofluid enhancement and confirms that the PINN captures physically consistent heat transfer trends in TPMS heat exchangers.

Figure 9 provides a three-dimensional visualization of the PINN-predicted temperature field mapped onto the TPMS gyroid surface for the aluminum sample at $Q = 19.85$ cm^3/s. In the present model, the full three-dimensional TPMS thermal behaviour is represented using a two-dimensional x-z temperature field. This means that the PINN predicts the temperature variation along the streamwise direction (x) and vertical heat transfer direction (z), while variations across the lateral direction (y) are not solved independently. The resulting x-z temperature field is then projected onto the three-dimensional TPMS geometry to visualize how the predicted thermal distribution appears on the complex gyroid surface.

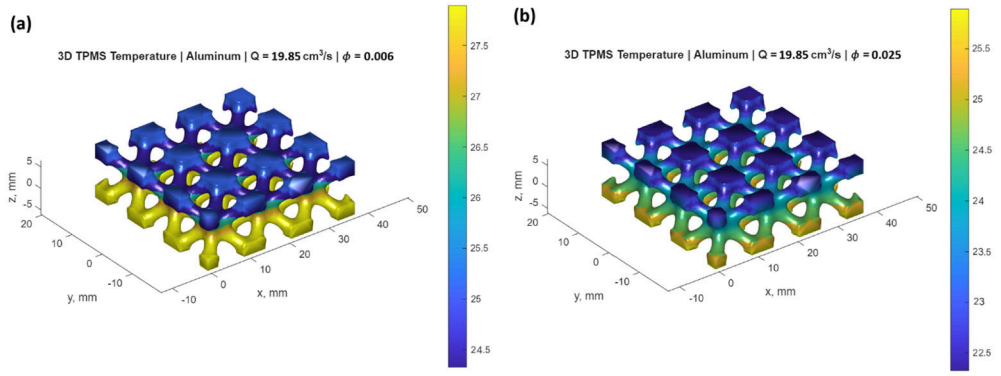

Figure 9. Three-dimensional mapping of the PINN-predicted x-z temperature field onto the aluminum TPMS gyroid surface at Q = 19.85 cm^3/s: (**a**) reference nanofluid concentration ϕ = 0.006; (**b**) higher nanoparticle concentration ϕ = 0.025.

Figure 9a corresponds to the reference nanofluid concentration $\varphi = 0.6\%$ vol, while Figure 9b corresponds to $\varphi = 2.5\%$ vol. The comparison between the two figures shows that increasing nanoparticle concentration reduces the overall temperature level on the TPMS. At $\varphi = 0.6\%$ vol, higher-temperature regions remain more pronounced near the lower heated portion of the structure, whereas at $\varphi = 2.5\%$ vol, the temperature distribution shifts toward lower values and becomes more thermally moderated.

This behaviour agrees with the thermocouple temperature profiles shown in Figures 6–8, where increasing nanoparticle concentration consistently reduced the predicted surface temperature. The 3D visualization should therefore be interpreted as a geometric mapping of the PINN-predicted x-z temperature field rather than a fully resolved three-dimensional CFD temperature solution. Nevertheless, it provides useful physical insight into how nanofluid concentration affects the spatial thermal response of the TPMS structure and helps connect the one-dimensional thermocouple profiles with the complex three-dimensional gyroid geometry.

Figure 10 illustrates the combined influence of volumetric flow rate and nanoparticle concentration on the PINN-predicted mean temperature for the aluminum and silver TPMS heat exchangers. For both materials, increasing the flow rate leads to a clear reduction in mean temperature. This trend is expected because higher flow rates strengthen forced convection inside the TPMS channels, allowing the working fluid to remove heat more

effectively from the solid structure. As the flow rate increases, the thermal boundary layer becomes thinner and the convective heat transfer coefficient increases, resulting in lower average surface temperatures.

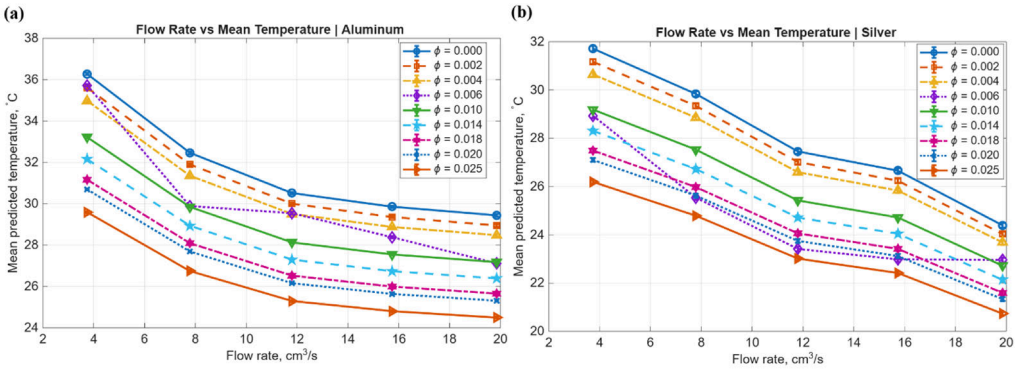

Figure 10. Effect of volumetric flow rate and nanoparticle volume fraction on the PINN-predicted mean temperature for TPMS heat exchangers: (**a**) aluminum sample and (**b**) silver sample.

At a fixed flow rate, increasing nanoparticle concentration generally lowers the predicted mean temperature because the enhanced effective thermal conductivity improves heat diffusion and strengthens heat transfer between the TPMS and the coolant.

This confirms the temperature-reduction trend discussed in Figures 6–8, where increasing φ from 0 to 2.5% vol produced an approximate temperature reduction of 17.5–18.5%. The effect is more noticeable at low and moderate flow rates, where the longer residence time allows the enhanced nanofluid properties to contribute more strongly to heat removal. At higher flow rates, forced convection becomes dominant, so the additional benefit of increasing φ becomes less pronounced. The figure confirms the temperature-reduction trend discussed earlier, where increasing the nanoparticle concentration reduced the predicted temperature. When this concentration increase was combined with increasing the flow rate from 3.74 to 19.85 cm^3/s the overall temperature reduction reached approximately 33.5%.

The silver TPMS sample shows lower mean temperatures than aluminum under similar conditions due to its higher thermal conductivity, which improves heat spreading through the solid structure and enhances thermal coupling with the nanofluid. This confirms that the thermal performance depends on both the coolant properties and the TPMS material conductivity.

However, increasing nanoparticle concentration also has drawbacks. Higher φ increases nanofluid viscosity, which can reduce flow mobility, increase pressure drop, and require higher pumping power in the tortuous TPMS channels. At high concentrations, the heat transfer benefit may become limited because thermal conductivity enhancement gives diminishing returns while viscosity continues to rise. Excessive nanoparticle loading may also cause agglomeration or sedimentation, reducing stability and increasing the risk of non-uniform flow or clogging. Therefore, an optimum concentration should balance heat transfer enhancement with viscosity, pressure drop, and suspension stability.

5.3. Convective Heat Transfer Performance and Heat-Removal Index

The heat-removal index provides an additional measure of overall thermal performance by combining the effects of heat transfer coefficient, heat transfer area, and the predicted temperature difference. Figure 11 compares the heat-removal index for aluminum and silver as a function of nanoparticle concentration at different flow rates. For both materials, the heat-removal index is strongly affected by flow rate, with higher flow rates producing larger values. This confirms that forced convection is the dominant mechanism controlling heat extraction in the TPMS channels.

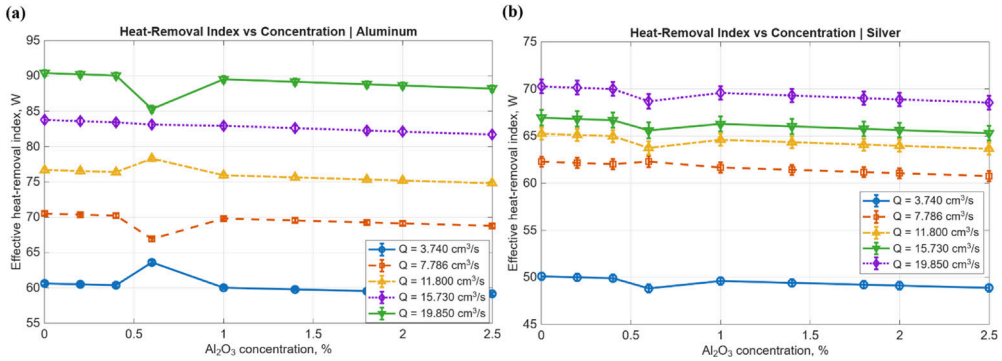

Figure 11. Effective heat-removal index as a function of Al_2O_3 nanoparticle concentration at different volumetric flow rates for TPMS heat exchangers: (**a**) aluminum sample and (**b**) silver sample.

A quantitative comparison was also conducted using the relative difference formulation given in Equation (42) between the pure-water case $\varphi = 0$ and the highest nanofluid concentration $\varphi = 2.5\%$ vol. The results show that the effective heat-removal index presented in Equation (33) changes by an average of approximately $q_{index} = 3$ W as the nanoparticle concentration increases from $\varphi = 0$ to $\varphi = 2.5\%$ vol. This relatively small variation occurs because the heat-removal index depends not only on h_{eff}, but also on the temperature difference between the TPMS and the inlet fluid. As nanoparticle concentration increases, h_{eff} increases due to improved convective heat transfer; however, T_{mean} decreases, which reduces the thermal driving temperature difference. These two effects partly offset each other. Therefore, the observed variation indicates that nanoparticle addition improves the local heat transfer coefficient, while the overall heat-removal index is governed by a balance between enhanced convection and the reduced temperature driving force.

Unlike the effective heat transfer coefficient, the heat-removal index does not increase monotonically with nanoparticle concentration. In several cases, it remains nearly constant or slightly decreases as concentration increases. This behaviour occurs because nanoparticle addition lowers the predicted TPMS temperature, which reduces the temperature difference between the solid surface and the inlet fluid. Therefore, the heat-removal index reflects the combined effect of an improved convective coefficient and reduced thermal driving potential. The comparison between aluminum and silver further demonstrates the influence of solid thermal conductivity on the heat-removal index. In the present results, aluminum generally shows larger heat-removal-index values because it is predicted that surface temperatures remain relatively higher, producing a larger temperature difference relative to the inlet fluid. Silver, on the other hand, maintains lower surface temperatures due to its higher thermal conductivity, which improves heat spreading and temperature uniformity within the TPMS structure. However, this also reduces the thermal driving temperature difference used in the heat-removal-index calculation. Therefore, differences in the heat-removal index should be interpreted together with the temperature profiles: Aluminum provides a larger driving temperature difference, while silver provides stronger temperature suppression and more uniform thermal behaviour.

Figure 11 also reveals that the heat-removal index is strongly influenced by flow rate, with higher flow rates producing larger values. This confirms that forced convection is the dominant mechanism controlling heat extraction within the TPMS channels. Collectively, these results show that the PINN-based framework captures the coupled effects of Reynolds number, nanoparticle concentration, and material conductivity on TPMS heat transfer performance.

Increasing the flow rate consistently improves convective transport, while increasing nanoparticle concentration enhances the effective heat transfer coefficient h_{eff}. However,

the improvement in the heat-removal index becomes limited at higher concentrations because the reduced surface temperature also lowers the available thermal driving force. Therefore, the optimum nanofluid concentration should be selected by balancing heat transfer enhancement with the resulting temperature difference, rather than relying only on the maximum value of h.

The small non-monotonic variations in Figure 11a result from the competing concentration-dependent terms in the effective heat-removal rate.

Nanoparticle addition increases the effective heat transfer coefficient but simultaneously reduces the predicted TPMS temperature and, hence, the available wall-to-fluid temperature difference.

Because the heat-removal rate is proportional to the product $h_{eff} A_s (T_s - T_f)$, an increase in h_{eff} may be partly or fully offset by a reduction in the thermal driving force. The resulting trend, therefore, reflects the coupled transport behaviour represented by the model rather than a direct monotonic dependence on nanoparticle concentration.

The convective heat transfer performance was evaluated using the PINN-predicted temperature fields and the corresponding nanofluid thermophysical properties. Figure 12 presents the enhanced effective heat transfer coefficient, h_{eff}, as a function of Al_2O_3 nanoparticle concentration for the aluminum TPMS sample at different volumetric flow rates. The results show that h_{eff} increases consistently as the nanoparticle concentration increases from $\varphi = 0$ to 2.5% vol. This trend confirms that adding nanoparticles improves the convective heat transfer capability of the working fluid.

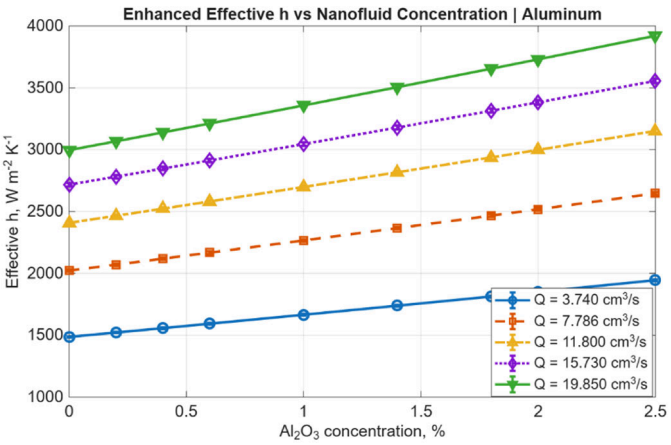

Figure 12. Enhanced effective heat transfer coefficient, h_{eff}, as a function of Al_2O_3 nanoparticle concentration at different volumetric flow rates for the aluminum TPMS heat exchanger.

At a fixed flow rate, the increase in h_{eff} is mainly attributed to the enhancement of the nanofluid effective thermal conductivity. As the Al_2O_3 concentration increases, heat diffusion within the fluid improves, and the thermal interaction between the TPMS solid surface and the flowing coolant becomes stronger. Figure 12 shows that the flow rate has a strong influence on h_{eff}. Higher flow rates produce larger effective heat transfer coefficients because stronger forced convection reduces the thermal boundary layer thickness and enhances heat exchange inside the TPMS channels.

A quantitative comparison using Equation (42) shows that, at a fixed concentration, increasing the flow rate improves h_{eff} by approximately 50.39%, while at a fixed flow rate, increasing the nanoparticle concentration improves h_{eff} by approximately 23.57%. When the concentration effect was combined with increasing the flow rate, the overall improvement reached about 62.08%.

This confirms that both nanoparticle concentration and flow rate contribute to convective enhancement, with flow rate producing the stronger overall effect in the present

results. It should also be noted that Figure 12 is presented for the aluminum sample only because, in the present formulation, h_{eff} is mainly governed by the heat transfer balance, nanofluid properties, flow rate, and geometry. The solid thermal conductivity k_s does not directly control the concentration-based variation in h_{eff} in this plot. Therefore, the silver case is expected to follow a similar trend, while material-dependent effects are more clearly reflected in the temperature profiles and heat-removal-index results.

5.4. Nusselt Number Enhancement and Scaling Behaviour

Figure 13a,b presents the variation in the effective Nusselt number with nanoparticle concentration and equivalent Reynolds number for the aluminum TPMS heat exchanger. The Nusselt number was evaluated from the effective heat transfer coefficient using the rearranged form of Equation (32). In this formulation, the Nusselt number represents the combined effects of convective heat transfer, flow conditions, nanofluid thermophysical properties, and TPMS geometry.

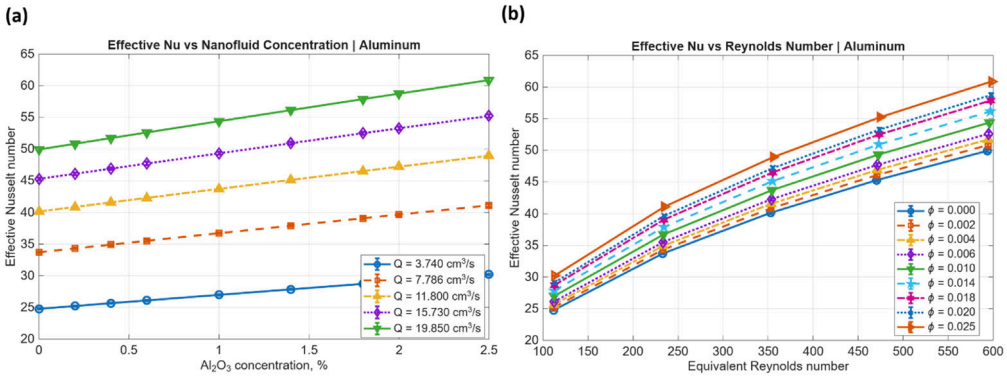

Figure 13. Effective Nusselt number variation for the aluminum TPMS heat exchanger: (**a**) effective Nusselt number as a function of Al_2O_3 nanoparticle concentration at different volumetric flow rates; (**b**) effective Nusselt number as a function of equivalent Reynolds number at different nanoparticle concentrations.

Figure 13a shows that the effective Nusselt number increases with Al_2O_3 concentration for all investigated flow rates. At a fixed flow rate, increasing nanoparticle concentration improves the thermal transport capability of the working fluid, which consequently increases Nu by approximately 17.98% as the concentration rises from $\varphi = 0$ to $\varphi = 2.5\%$ vol.

The lowest Nusselt numbers are observed for pure water $\varphi = 0$, while the highest values occur at the maximum nanoparticle concentration $\varphi = 2.5\%$ vol. This confirms that nanofluid addition enhances convective heat transfer performance inside the TPMS channels.

The influence of flow rate is also evident in Figure 13a. Higher volumetric flow rates produce higher Nusselt numbers, with an improvement of approximately 50.39% across the investigated flow-rate range. This behaviour is consistent with forced convection theory, where increasing the flow rate increases the Reynolds number, reduces the thermal boundary layer thickness, and strengthens heat exchange between the TPMS and the coolant.

Nonlinear behaviour is observed between the Nusselt number and Reynolds number, as shown in Figure 13b. At the same Reynolds number, higher Al_2O_3 concentrations produce higher Nusselt numbers, confirming the additional contribution of nanofluid thermal enhancement beyond flow-driven convection.

Increasing the concentration from $\varphi = 0$ to 2.5% vol improves Nu by approximately 17.98%. This effect becomes more pronounced at higher flow intensity: a low Reynolds number, Nu increases from 24.77 to 30.20, while at $Re \approx 600$, Nu increases from 49.93.

Overall, combining the nanoparticle-concentration increase with the flow-rate increase improves the effective Nusselt number by approximately 58.33% and increases the Reynolds number by approximately 59.32%.

The nonlinear trend shows that heat transfer enhancement is controlled by both nanoparticle concentration and flow intensity. Al_2O_3 addition improves Nu, but its effect becomes more significant at higher Reynolds numbers because stronger flow enhances convective transport inside the TPMS channels. Although the Nusselt number increases with concentration, the enhancement should not be interpreted as purely material-dependent.

In the present formulation, Nu is governed mainly by h_{eff}, k_{nf} flow rate φ, and hydraulic diameter D_h, while the solid thermal conductivity k_s does not explicitly appear in the Nusselt number calculation. For this reason, the aluminum case is used as the representative material for the Nusselt number analysis. The silver case is expected to follow a similar scaling trend, while material-dependent effects are more clearly reflected in the temperature profiles and heat-removal-index results.

The results also show that the Nusselt number increases more smoothly with concentration than the temperature reduction trends. This is because the Nusselt number is directly linked to the effective heat transfer coefficient, whereas the temperature and heat-removal-index results also depend on the thermal driving temperature difference. Therefore, increasing nanoparticle concentration can improve Nu while producing smaller gains in the overall heat-removal index. This highlights the need to interpret Nusselt number enhancement together with temperature reduction, heat-removal capacity, viscosity effects, and pumping-power requirements.

Ultimately, Figure 13a,b demonstrates that both Reynolds number and nanoparticle concentration enhance the convective heat transfer performance of the TPMS heat exchanger. The PINN-based framework captures these physically consistent trends by combining learned temperature-field reconstruction with thermos-physical-property-based heat transfer post-processing. This supports the use of the proposed model for evaluating nanofluid-enhanced TPMS heat exchangers across different flow and concentration conditions.

5.5. Implications for TPMS Heat Exchanger Design

The results demonstrate that nanofluid-enhanced TPMS heat exchangers exhibit optimal operating regimes in which thermal performance gains are maximized while viscosity-induced penalties remain limited. The PINN framework enables rapid exploration of this design space by predicting thermal behaviour across a wide range of nanoparticle concentrations and flow rates without requiring additional experiments or computationally expensive simulations.

From a practical perspective, the findings suggest that moderate nanoparticle concentrations provide the most favourable trade-off between heat transfer enhancement and hydrodynamic performance. Excessive concentrations may produce diminishing thermal returns, particularly in highly tortuous TPMS geometries, where increased viscosity can raise pressure drop and pumping-power requirements. Therefore, the selection of nanofluid concentration should consider not only the enhancement in h_{eff} and Nu, but also the associated changes in mean temperature, heat-removal capacity, and flow resistance.

In essence, the present results confirm that the proposed PINN-based approach can provide physically consistent predictions of nanofluid heat transfer in TPMS heat exchangers. The model successfully captures the coupled effects of flow rate, nanoparticle concentration, and material conductivity on temperature distribution and convective performance. These insights provide a useful basis for optimizing next-generation TPMS heat exchangers and selecting appropriate working-fluid formulations for improved thermal management.

5.6. Limitations of Concentration Extrapolation

The proposed framework combines a PINN trained using experimental measurements at pure water and the reference nanofluid concentration $\varphi_{ref} = 0.6\%$ with a physics-based concentration scaling model to predict thermal behaviour at other nanoparticle concentrations. Consequently, the predictive capability outside the training conditions depends on the validity of the concentration scaling model rather than on direct learning from experimental data.

The extrapolation assumes that the governing heat transfer mechanisms remain unchanged throughout the investigated concentration range and that the nanofluid can be represented as a homogeneous single-phase effective medium. It is further assumed that the concentration-dependent variations in density, viscosity, specific heat, and thermal conductivity are adequately described by the adopted effective-property correlations. Under these assumptions, the Reynolds number, Prandtl number, and effective thermal conductivity remain the dominant parameters controlling convective heat transfer.

As the nanoparticle concentration increases, additional phenomena such as particle agglomeration, sedimentation, non-uniform dispersion, changes in rheological behaviour, and fouling may become increasingly important. These effects are not explicitly represented in the present concentration scaling model and may reduce prediction accuracy at concentrations significantly higher than the experimental reference condition. Consequently, the present framework should be regarded as most reliable within the investigated concentration range, while predictions obtained farther from the training concentration should be interpreted with appropriate caution until validated using independent experimental measurements.

Because the available experimental dataset was intentionally limited, all measured temperatures were used during training to maximize the information available for learning the governing thermal physics. The physics-informed loss evaluated at the collocation points acted as an intrinsic regularization mechanism by constraining the solution to satisfy the governing energy equation throughout the computational domain. Consequently, the reported RMSE reflects reconstruction accuracy rather than independent predictive accuracy. Future work will include additional experimental datasets acquired at different nanoparticle concentrations and operating conditions to enable independent validation and more rigorous assessment of the model generalization capability.

6. Conclusions

This study developed a hybrid physics-informed neural network (PINN) framework for predicting nanofluid thermal transport in TPMS gyroid heat exchangers using sparse experimental measurements. The framework integrates experimental thermocouple data, the governing convection–diffusion equation, concentration-dependent nanofluid property models, and a physics-based concentration scaling approach. The PINN reconstructs the reference TPMS temperature field, while the effective heat transfer coefficient and Nusselt number are subsequently evaluated from the predicted temperatures using an energy balance formulation.

The proposed framework accurately reconstructed the experimental temperature field, yielding a reconstruction RMSE of 0.028 °C, a MAPE of 0.0899%, and an R2 value of 0.99994. Excellent agreement between the reconstructed and measured temperature profiles was obtained for both aluminum and silver TPMS heat exchangers, demonstrating the capability of the proposed framework to capture the thermal behaviour of the investigated system.

The results showed that increasing nanoparticle concentration and volumetric flow rate enhanced the thermal performance of the TPMS heat exchanger. The combined effect reduced the predicted TPMS temperature by approximately 33.5% and increased the effective

heat transfer coefficient, Nusselt number, and Reynolds number by approximately 62.08%, 58.33%, and 59.32%, respectively. The silver TPMS produced lower and more uniform temperatures because of its higher thermal conductivity, whereas the aluminum TPMS exhibited a greater heat-removal capacity owing to its larger wall-to-fluid temperature difference, highlighting that lower surface temperature and higher heat-removal capacity are not necessarily equivalent measures of thermal performance.

The LTE–LTNE sensitivity analysis confirmed that the local thermal equilibrium assumption is appropriate for the investigated TPMS geometry and operating conditions, with only minor differences observed between the LTE and LTNE predictions. Overall, the proposed hybrid PINN framework provides a computationally efficient and physically consistent surrogate model for evaluating nanofluid-enhanced TPMS heat exchangers while substantially reducing the need for extensive experimentation and computationally expensive numerical simulations. Future work will focus on validating the framework using additional experimental datasets at multiple nanoparticle concentrations, incorporating pressure-drop measurements and fully three-dimensional flow fields, and extending the methodology to other nanofluids and TPMS architectures.

Author Contributions: Conceptualization, M.Y.; methodology, M.Y.; software, M.Y.; validation, M.Y.; formal analysis, M.Y. and M.Z.S.; investigation, M.Y. and M.Z.S.; data curation, M.Y. and M.Z.S.; writing the original draft preparation, review and editing; M.Y.; visualization; M.Y. and M.Z.S.; supervision, M.Z.S. All authors have read and agreed to the published version of the manuscript.

Funding: This research received no external funding.

Data Availability Statement: The original contributions presented in this study are included in the article. Further inquiries can be directed to the corresponding author(s).

Acknowledgments: The authors gratefully acknowledge the technical and laboratory support provided during the experimental work and development of the TPMS heat transfer test system.

Conflicts of Interest: The authors declare no conflicts of interest.

Nomenclature

T	Temperature °C
T_f	Nanofluid temperature
$\boldsymbol{T_s}$	Solid structure temperature
$\boldsymbol{T_{pred}}$	Predicted temperatures
$\boldsymbol{\varphi}$	Concertation
$\boldsymbol{\varphi_{ref}}$	Experiment reference concertation
$\boldsymbol{D_h}$	Hydraulic diameter
$\boldsymbol{\rho}$	Density kg/m^3
$\boldsymbol{C_P}$	Specific heat capacity
$\boldsymbol{h_{eff}}$	Heat transfer coefficient
$\boldsymbol{k}$	Thermal conductivity
$\boldsymbol{k_{eff}}$	Effective thermal conductivity
$\boldsymbol{k_s}$	Solid thermal conductivity
$\boldsymbol{k_{ref}}$	Reference thermal conductivity
$\boldsymbol{Q}$	Flow rate
$\boldsymbol{p_i}$	Measurement location index
$\boldsymbol{T_{mean}}$	Measured temperature
$\boldsymbol{\lambda}$	Regularization weight for optimization model
$\boldsymbol{Q(t)}$	Heat flux
$\boldsymbol{\Phi}$	Gyroid surface equation

$\mathcal{L}_{PDE}$	Quantifies the physics of the heat-conduction partial differential equation.
$\mathcal{L}_{data}$	PINN-predicted temperature matches the measured temperature data.
q''	Surface heat flux
q_{index}	Effective heat-removal index
N	Total number of material elements in the model.
$\mathcal{R}_{PDE}$	Physics residual of the governing energy equation
Nu	Nusselt number
Nu_{base}	Base or reference Nusselt number
D_h	Hydraulic diameter
A_f	Fluid-filled cross-sectional area
R_e	Reynolds number
P_e	Péclet number
u_p	Pore velocity
u_{avg}	Average velocity
σ_T	Standard deviation
μ	Dynamic viscosity

References

1. Sekulic, D.P.; Shah, R.K. *Fundamentals of Heat Exchanger Design*; John Wiley & Sons: Hoboken, NJ, USA, 2023. [CrossRef]
2. Thulukkanam, K. *Heat Exchangers: Classification, Selection, and Thermal Design*; CRC Press: Boca Raton, FL, USA, 2024. [CrossRef]
3. Ajeeb, W.; Murshed, S.S. Comparisons of numerical and experimental investigations of the thermal performance of Al2O3 and TiO2 nanofluids in a compact plate heat exchanger. *Nanomaterials* **2022**, *12*, 3634. [CrossRef] [PubMed]
4. Saghir, M.Z.; Yahya, M. Convection heat transfer and performance analysis of a triply periodic minimal surface (TPMS) for a novel heat exchanger. *Energies* **2024**, *17*, 4275. [CrossRef]
5. Al-Ketan, O.; Abu Al-Rub, R.K. MSLattice: A free software for generating uniform and graded lattices based on triply periodic minimal surfaces. *Mater. Des. Process. Commun.* **2021**, *3*, e205. [CrossRef]
6. Qian, C.; Wang, J.; Zhong, H.; Qiu, X.; Yu, B.; Shi, J.; Chen, J. Experimental investigation on heat transfer characteristics of copper heat exchangers based on triply periodic minimal surfaces (TPMS). *Int. Commun. Heat Mass Transf.* **2024**, *152*, 107292. [CrossRef]
7. Reynolds, B.W.; Fee, C.J.; Morison, K.R.; Holland, D.J. Characterisation of heat transfer within 3D printed TPMS heat exchangers. *Int. J. Heat Mass Transf.* **2023**, *212*, 124264. [CrossRef]
8. Beer, M.; Rybár, R. Optimisation of heat exchanger performance using modified Gyroid-based TPMS structures. *Processes* **2024**, *12*, 2943. [CrossRef]
9. Wang, J.; Qian, C.; Zhang, F.; Qiu, X.; Yu, B.; Shi, J.; Chen, J. Experimental and numerical analysis of functionally graded hybrid TPMS heat exchangers for enhanced flow and thermal performance. *Appl. Therm. Eng.* **2025**, *264*, 125528. [CrossRef]
10. Wang, J.; Qian, C.; Qiu, X.; Yu, B.; Yan, L.; Shi, J.; Chen, J. Numerical and experimental investigation of additive manufactured heat exchanger using triply periodic minimal surfaces (TPMS). *Therm. Sci. Eng. Prog.* **2024**, *55*, 10300. [CrossRef]
11. Kilic, G. Performance evaluation of triply periodic minimal surface heat exchangers using nanofluids at high flow rates for enhanced energy efficiency. *Appl. Sci.* **2025**, *15*, 4140. [CrossRef]
12. Saghir, M.Z.; Kilic, G.A. Experimental forced convection study using a triply periodic minimal surface porous structure with a nanofluid: Comparison with numerical modeling. *Appl. Sci.* **2024**, *14*, 7594. [CrossRef]
13. Mohammed, H.; Bhaskaran, G.; Shuaib, N.; Saidur, R. Heat transfer and fluid flow characteristics in microchannels heat exchanger using nanofluids: A review. *Renew. Sustain. Energy Rev.* **2011**, *15*, 15021512. [CrossRef]
14. Albadr, J.; Tayal, S.; Alasadi, M. Heat transfer through heat exchanger using Al2O3 nanofluid at different concentrations. *Case Stud. Therm. Eng.* **2013**, *1*, 38–44. [CrossRef]
15. Ghazanfari, V.; Taheri, A.; Amini, Y.; Mansourzade, F. Enhancing heat transfer in a heat exchanger: CFD study of twisted tube and nanofluid (Al2O3, Cu, CuO, and TiO2) effects. *Case Stud. Therm. Eng.* **2024**, *53*, 103864. [CrossRef]
16. Pattanayak, B.; Mund, A.; Jayakumar, J.S.; Parashar, K.; Parashar, S.K.S. Estimation of Nusselt number and effectiveness of double-pipe heat exchanger with Al2O3–, CuO–, TiO2–, and ZnO– water based nanofluids. *Heat Transf.* **2020**, *49*, 2228–2247. [CrossRef]
17. Zahmani, Q.F.; Asmuin, N.; Sued, M.K.; Mokhtar, S.N.; Sahar, M.N.H. Nanofluid-infused microchannel heat sinks: Comparative study of Al2O3, TiO2, and CuO to optimized thermal efficiency. *J. Adv. Res. Micro Nano Eng.* **2024**, *19*, 1–12. [CrossRef]
18. Ansari, A.J.; Maurya, A.K. Nanofluid Flows in Heat Exchangers. In *Advances in Computational Fluid Dynamics*; CRC Press: Boca Raton, FL, USA, 2025. [CrossRef]

19. Vajjha, R.S.; Das, D.K. A review and analysis on influence of temperature and concentration of nanofluids on thermophysical properties, heat transfer and pumping power. *Int. J. Heat Mass Transf.* **2012**, *55*, 4063–4078. [CrossRef]
20. Vafai, K. (Ed.) *Handbook of Porous Media*; CRC Press: Boca Raton, FL, USA, 2015. [CrossRef]
21. Akbari, P.; Zamani, M.; Mostafaei, A. Machine learning prediction of mechanical properties in metal additive manufacturing. *Addit. Manuf.* **2024**, *91*, 104320. [CrossRef]
22. Deng, Z.-H.; Yin, H.-Q.; Jiang, X.; Zhang, C.; Zhang, G.-F.; Xu, B.; Yang, G.-Q.; Zhang, T.; Wu, M.; Qu, X.-H. Machine-learning-assisted prediction of the mechanical properties of Cu-Al alloy. *Int. J. Miner. Metall. Mater.* **2020**, *27*, 362–373. [CrossRef]
23. Imran, M.; Amjad, H.; Khan, S.; Ali, S. Machine learning assisted prediction of the mechanical properties of carbon nanotube-incorporated concrete. *Struct. Concr.* **2015**, *26*, 1613–1635. [CrossRef]
24. Ewim, D.R.E.; Okwu, M.O.; Onyiriuka, E.J.; Abiodun, A.S.; Abolarin, S.M.; Kaood, A. A quick review of the applications of artificial neural networks (ANN) in the modelling of thermal systems. *Eng. Appl. Sci. Res.* **2021**, *49*, 444–458. [CrossRef]
25. Ibrahim, M.; Saeed, T.; Algehyne, E.A.; Berrouk, A.S.; Chu, Y.-M. Numerical investigation and ANN modeling of the effect of single-phase and two-phase analysis of convective heat transfer of nanofluid in a cavity. *J. Therm. Anal. Calorim.* **2021**, *145*, 1969–1991. [CrossRef]
26. Raissi, M.; Perdikaris, P.; Karniadakis, G.E. Physics-informed neural networks: A deep learning framework for solving forward and inverse problems involving nonlinear partial differential equations. *J. Comput. Phys.* **2019**, *378*, 686–707. [CrossRef]
27. Cuomo, S.; Di Cola, V.S.; Giampaolo, F.; Rozza, G.; Raissi, M.; Piccialli, F. Scientific machine learning through physics–informed neural networks: Where we are and what's next. *J. Sci. Comput.* **2022**, *92*, 88. [CrossRef]
28. Uhrich, B.; Pfeifer, N.; Schäfer, M.; Theile, O.; Rahm, E. Physics-informed deep learning to quantify anomalies for real-time fault mitigation in 3D printing. *Appl. Intell.* **2024**, *54*, 4736–4755. [CrossRef]
29. Yahya, M.; Saghir, M.Z. Machine Learning and Physics-Informed Neural Networks for Thermal Behavior Prediction in Porous TPMS Metals. *Fluids* **2026**, *11*, 29. [CrossRef]
30. El Hassan, M.; Mjalled, A.; Miron, P.; Mönnigmann, M.; Bukharin, N. Machine Learning in Fluid Dynamics-Physics-Informed Neural Networks (PINNs) Using Sparse Data: A Review. *Fluids* **2025**, *10*, 226. [CrossRef]
31. Zhang, W.; Xie, X.; Pan, H.; Duan, X.; Sun, B.; Du, Q.; Lu, L. MUSA-PINN: Multi-scale Weak-form Physics-Informed Neural Networks for Fluid Flow in Complex Geometries. *arXiv* **2026**, arXiv:2603.08465. [CrossRef]
32. Bobbili, V.S.R.; Sastry, C.C.; Krishnaiah, J.; Rahman, A.H.; Kumar, S.S.; Reddy, N.S. Physics-informed neural networks for predicting high-strain-rate energy absorption in additively manufactured lattice materials. *Prog. Addit. Manuf.* **2026**, *11*, 2095–2121. [CrossRef]
33. Schläfli, L.; Steiner-Schläfli-Komitee. *Gesammelte Mathematische Abhandlungen*; Birkhäuser: Basel, Switzerland, 1950. [CrossRef]
34. Gandy, P.J.; Bardhan, S.; Mackay, A.L.; Klinowski, J. Nodal surface approximations to the P, G, D and I-WP triply periodic minimal surfaces. *Chem. Phys. Lett.* **2001**, *336*, 187–195. [CrossRef]
35. Kaur, I.; Singh, P. State-of-the-art in heat exchanger additive manufacturing. *Int. J. Heat Mass Transf.* **2021**, *178*, 121600. [CrossRef]
36. Yahya, M.; Yahya, A.; Saghir, M.Z. Experimental Measurement and Numerical Modelling of Solid Network-Based Schoen's I-Graph—Wrapped Package (I-WP) toward Cooling Heat Sink. *Therm. Sci. Appl.* **2025**, *1*, 3–20. [CrossRef]
37. Li, L.; Iskander, M. Visualization of interstitial pore fluid flow. *J. Imaging* **2022**, *8*, 32. [CrossRef] [PubMed]
38. Arthur, J.K. Flow Through and over Model Porous Media with or Without Inertial Effects. Ph.D. Dissertation, University of Manitoba, Winnipeg, MB, Canada, 2012.
39. Nield, D.A.; Bejan, A. *Convection in Porous Media*; Springer: New York, NY, USA, 2006. [CrossRef]
40. Das, S.K.; Choi, S.U.; Yu, W.; Pradeep, T. *Nanofluids: Science and Technology*; John Wiley & Sons: Hoboken, NJ, USA, 2007. [CrossRef]
41. Gudkov, S.V.; Burmistrov, D.E.; Smirnova, V.V.; Semenova, A.A.; Lisitsyn, A.B. A mini review of antibacterial properties of Al_2O_3 nanoparticles. *Nanomaterials* **2022**, *12*, 2635. [CrossRef] [PubMed]
42. Eastman, J.A.; Choi, S.U.S.; Li, S.; Yu, W.; Thompson, L.J. Anomalously increased effective thermal conductivities of ethylene glycol-based nanofluids containing copper nanoparticles. *Appl. Phys. Lett.* **2001**, *78*, 718–720. [CrossRef]
43. Pak, B.C.; Cho, Y.I. Hydrodynamic and heat transfer study of dispersed fluids with submicron metallic oxide particles. *Exp. Heat Transf. Int. J.* **1998**, *11*, 151–170. [CrossRef]
44. Garoosi, F. Presenting two new empirical models for calculating the effective dynamic viscosity and thermal conductivity of nanofluids. *Powder Technol.* **2020**, *366*, 788–820. [CrossRef]
45. Brinkman, H. The viscosity of concentrated suspensions and solutions. *J. Chem. Phys.* **1952**, *20*, 571. [CrossRef]
46. Maxwell, J. *A Treatise on Electricity and Magnetism*; Clarendon Press: Oxford, UK, 1873; Volume 1.
47. Çengel, Y.A.; Ghajar, A.J. *Heat and Mass Transfer: Fundamentals and Applications*; McGraw-Hill: New York, NY, USA, 2015.
48. Kingma, D.P.; Ba, J. A methodforstochastic optimization. *arXiv* **2015**, arXiv:1412.6980.
49. Bergman, T.L. *Fundamentals of Heat and Mass Transfer*; John Wiley & Sons: Hoboken, NJ, USA, 2011.

50. Xuan, Y.; Li, Q. Investigation on convective heat transfer and flow features of nanofluids. *J. Heat Transf.* **2003**, *125*, 151–155. [CrossRef]
51. Islam, S.; Dutta, P. Machine learning assisted inverse heat transfer problem to find heat flux in ablative materials. *Mater. Today Commun.* **2025**, *45*, 112337. [CrossRef]